

Influences of Large-Scale Flow Variations on the Track Evolution of Typhoons Morakot (2009) and Megi (2010): Simulations with a Global Variable-Resolution Model

CHING-YUANG HUANG AND YOU ZHANG

Department of Atmospheric Sciences, National Central University, Jhong-Li, Taiwan

WILLIAM C. SKAMAROCK

National Center for Atmospheric Research, Boulder, Colorado

LI-HUAN HSU

Taiwan Typhoon and Flood Research Institute, National Applied Research Laboratories, Taipei, Taiwan

(Manuscript received 20 September 2016, in final form 7 February 2017)

ABSTRACT


Influences of large-scale flow variations on the track evolution of two typhoons, moderate Morakot (2009) and superintense Megi (2010), are investigated using the global variable-resolution model MPAS with a higher-resolution region of 15 km for the simulated typhoons. For Morakot, the associated track and extreme rainfall over southern Taiwan captured by MPAS compared well with the regional WRF simulations. To isolate the influences of various large-scale flows, three modes are filtered out from global reanalysis: the synoptic-scale mode, quasi-biweekly oscillation (QBW) mode, and the Madden–Julian oscillation (MJO) mode. In the absence of QBW or MJO, the simulated Morakot moves westward across Taiwan without the observed north turn after landfall. When the intensity of the MJO mode is increased by 50% in the experiment (MJO+50%), a much earlier northward turn is induced. The simulated Morakot under the observed MJO lies in between MJO+50% and MJO−50% results. The MJO variations also show similar impacts on the track evolution of Typhoon Megi.

The wavenumber-1 decompositions of vorticity budget terms are shown to highlight important contributions to the vorticity tendency and typhoon translation with and without the MJO. The northward turn of both typhoons in the presence of the MJO is mainly in response to positive horizontal vorticity advection to the north of the typhoon center. However, vorticity tilting is relatively more important for Morakot due to its slantwise structure. Furthermore, positive vorticity stretching and vertical advection are significant in the vicinity of southern Taiwan due to the effects of the Central Mountain Range and tend to retard the departing Morakot.

1. Introduction

Located near the edge of Eurasia and in the western North Pacific, Taiwan is under the influence of the East Asia monsoon and suffers from three to four tropical cyclones (TCs) every year. The formation and motion of

TCs are significantly affected by the large-scale circulation established by the monsoon associated with the intraseasonal oscillations (ISO), including the quasi-biweekly oscillation (QBW) and the Madden–Julian oscillation (MJO) (Liebmann et al. 1994). Ko and Hsu (2009) found that the recurving TCs in the vicinity of Taiwan, likely as part of the wavelike pattern, are modulated by the ISO westerly phase, which provides a favorable environment for wave–TC pattern development. The different phases associated with the MJO exert distinct impacts on the tracks of tropical cyclones in the western North Pacific (Li and Zhou 2013). From composite analysis, Ling et al. (2016) showed that the

 Denotes content that is immediately available upon publication as open access.

Corresponding author e-mail: Prof. Ching-Yuang Huang, hcy@atm.ncu.edu.tw

ISO flow plays an important role in steering the motion of local tropical cyclones in summer over the South China Sea.

One of the catastrophic typhoons impinging Taiwan associated with the influences of ISO is Morakot (2011), which brought more than 2400 mm in 3 days over southern Taiwan. There exist complex interactions among the typhoon circulation of Morakot, the monsoon gyre, and the steep terrain of the Central Mountain Range (CMR) in Taiwan, especially when Morakot was departing from northern Taiwan in association with the enhanced southwesterly flow southwest of Taiwan (e.g., Chien and Kuo 2011; Wu et al. 2011; Wang et al. 2012). Hong et al. (2010) found that the record-breaking rainfall was primarily caused by interactions between Morakot and the submonthly large-scale cyclonic disturbance during the active phase of 40–50-day ISO. Liang et al. (2011) demonstrated that the multi-time-scale monsoonal flows may have influenced the track evolution of Typhoon Morakot based on sensitivity experiments using a regional model. The MJO mode of the environmental flow was found to lead to an earlier northward vortex drift and then a westward track about 150 km north of Taiwan. However, observational analyses tend to suggest a predominant role of the MJO mode in enhancing the southwesterly flow that possibly drives Morakot northward when departing from northern Taiwan (Ge et al. 2010; Hong et al. 2010; Wu et al. 2011).

Since the MJO mode is embedded in the environmental flow, the relative contributions of multiscale flow components to Morakot's movement may be explored more explicitly by conducting model simulations with different initial conditions without specific modes in the flow. In this study, a global model with variable resolution is utilized to simulate Morakot under the environment with and without specific large-scale modes, which complements the regional model simulations that are limited by the lateral extent of the model domain. To further understand how the large-scale modes influence the translation of Morakot, sensitivity experiments regarding the variations of the MJO mode were also conducted. This study provides a further understanding of how variations of the MJO mode may lead to a substantial change in the evolution of Morakot.

Besides Morakot, the movement of Supertyphoon Megi (2010) after crossing the Philippines at later stages was also greatly influenced by the MJO mode. The impact of the ISO on the evolution of Megi has been investigated using a regional model (Bi et al. 2015). The track evolution of Megi took place over the open ocean away from the Philippines, in contrast to that of Morakot over Taiwan with the high CMR. The later interaction of Megi with the CMR is important for

causing heavy rainfall over northeastern Taiwan (Chen and Wu 2016). In this study, we focus on the MJO impacts during the earlier stage near Megi's recurvature. The comparisons of the track evolution of both typhoons and their underlying mechanisms of recurvature in relation to the large-scale environmental flow and its variations help illuminate the mechanisms underlying the evolutions in our high-resolution global model simulations.

We should note herein that there are slightly different definitions of MJO and ISO. The MJO nowadays is referred to as the large-scale intraseasonal disturbances in winter/fall that originate from the Indian Ocean and propagate eastward into the western North Pacific. The MJO interacting with Morakot in summer may be regarded as an ISO (e.g., Hong et al. 2010). Bi et al. (2015) investigated the impact of ISO mode (10–60 days) on Megi. In this study, we focus on the impacts of the specific MJO mode (20–60 days) on the evolution of both typhoons. This MJO mode was also adopted by Liang et al. (2011).

The content of this paper is organized as follows. The model descriptions and configurations of both the global model and regional model, together with their experimental setups for Morakot, are given in section 2. An overview of the evolution of Typhoon Morakot and its interaction with the monsoonal flow are presented in section 3. The simulated results for Typhoon Morakot are presented in sections 4. For comparison, Typhoon Megi and its simulations are given in section 5. We will show the influences of the MJO and its variations on the track evolution of the two typhoons and discuss the dynamics of the vortex movement based on diagnostics of the vorticity tendency budget in each section. Section 6 contains a further discussion concerning the differences in the movement of the two distinct typhoons. Wavenumber decompositions of the typhoon circulation and vorticity tendency budget will be provided to highlight the physical processes in the typhoon movement. Conclusions are given in section 7.

2. Models and experimental configurations

a. The MPAS model

The global model used in this study is the Model for Prediction Across Scales (MPAS), version 4.0. MPAS is a nonhydrostatic global atmosphere model developed at NCAR (Skamarock et al. 2012). The notable advantage of MPAS is the use of unstructured centroidal Voronoi mesh (grid, or tessellation) as the basis for the horizontal discretization in the fluid-flow solver, thus allowing for variable resolution. The unstructured variable-resolution meshes can be generated with smoothly varying mesh transitions and this capability ameliorates many issues

associated with the traditional mesh refinement strategies of one-way and two-way grid nesting employing regional models, where the transitions are abrupt (Skamarock et al. 2012; Hagos et al. 2013; Park et al. 2014).

The MPAS atmospheric dynamical core solves the fully compressible nonhydrostatic equations of motion. The horizontal Voronoi mesh uses a C-grid staggering of the state variables; the horizontal velocity is defined as the normal velocity on Voronoi cell faces, while the other state variables are defined at the cell centers where they represent cell-averaged values in the finite-volume formulation. The vertical momentum is prognostic and defined on the vertical cell faces located half a grid level above and below the cell center, consistent with a 3D C-grid discretization (Skamarock et al. 2012).

The MPAS-Atmosphere solver can use both a traditional terrain-following height coordinate and a generalized hybrid coordinate that can be configured to relax to a constant height coordinate at an intermediate height below the lid. The hybrid coordinate has the option of preferentially filtering the small-wavelength features of topography in its terrain-following coordinate region. In the formulation of the hybrid coordinate, the height of the coordinate surface is defined by

$$z = \zeta + A(\zeta)h_s(x, y, \zeta), \quad (1)$$

where ζ represents the nominal heights (ignoring terrain) of the coordinate surfaces; $A(\zeta)$ controls the rate at which the coordinate transitions from terrain following at the surface toward constant height surfaces aloft; and $h_s(x, y, \zeta)$ represents the terrain influence in the vertical-coordinate definition with the requirement that $h_s(x, y, 0) = h(x, y)$, where $h(x, y)$ is the surface terrain. Compared with traditional formulations, this hybrid terrain-following formulation can significantly reduce artificial circulations caused by inaccuracies in the horizontal pressure gradient term (Klemp 2011).

A 60–15-km variable-resolution MPAS mesh is used in this study where the higher resolution of 15 km is centered over the Taiwan area and covers the entirety of East Asia as shown in Fig. 1a. In the numerical simulations, the model physics includes the Weather Research and Forecasting (WRF) Model single-moment 6-class microphysics scheme (WSM6), the Tiedtke convective cumulus scheme, Yonsei University (YSU) planetary boundary layer parameterization, Monin–Obukhov surface layer parameterization, the Noah land surface model, and the Rapid Radiative Transfer Model for GCM applications (RRTMG) longwave and shortwave radiation parameterizations. References for these physical schemes can be found in the technical note (Skamarock et al. 2008) (available online at <http://wrf-model.org>). The

initial conditions were taken from the European Centre for Medium-Range Weather Forecasts interim reanalysis (ERA-Interim) on $0.5^\circ \times 0.5^\circ$ grids for Typhoon Morakot. All of the numerical simulations start at 0000 UTC 6 August 2009, and are integrated for 96 h covering the major phase of Morakot that strongly affected Taiwan. During the model integration, the sea surface temperature is kept unchanged.

b. The WRF Model

It has been well recognized that the lateral boundary conditions used for a regional model will significantly affect the evolution of a tropical cyclone (Hack and Schubert 1981). The global model MPAS simulates the long-term track evolution of a typhoon without impacts from any lateral boundary conditions. For comparisons with the global model simulations with variable resolution for Morakot, we also utilized the Advanced Research version of the regional WRF model (Skamarock et al. 2008). The initial conditions and model physics used in the WRF simulations are the same as in the MPAS simulations. For enhancing the horizontal resolution, the WRF simulations employ nested domains (see Table 1). In WRF-5km, the simulation includes three two-way interactive domains with horizontal resolutions of 45, 15, and 5 km, respectively, as shown in Fig. 1b. In WRF-15km, the simulation includes the same domains as in WRF-5km, but without the innermost domain of 5-km resolution. The lateral boundary conditions for WRF are also from the ERA-Interim, which are updated every 6 h.

3. Morakot event and its associated large-scale flow

a. Typhoon Morakot

The category 2 Typhoon Morakot is the most catastrophic typhoon in the recorded history of Taiwan. It formed early as a tropical depression east of the northern Philippines within a monsoon trough on 2 August 2009. The depression gradually developed and strengthened into a tropical storm late on 4 August, and then it became a typhoon in the morning of 5 August, named Morakot. The system continued to intensify as it moved westward toward Taiwan. Early on 7 August, Morakot reached its peak category 2 intensity with a minimum central pressure of 945 hPa and sustained winds of 85 kt (~ 98 mph) near its center. Morakot made landfall at eastern Taiwan later on 7 August and took more than 15 h to pass over Taiwan.

According to the best track (shown later) from the Central Weather Bureau (CWB) of Taiwan, Morakot headed toward Taiwan under the influence of the subtropical high over the western North Pacific. An area of

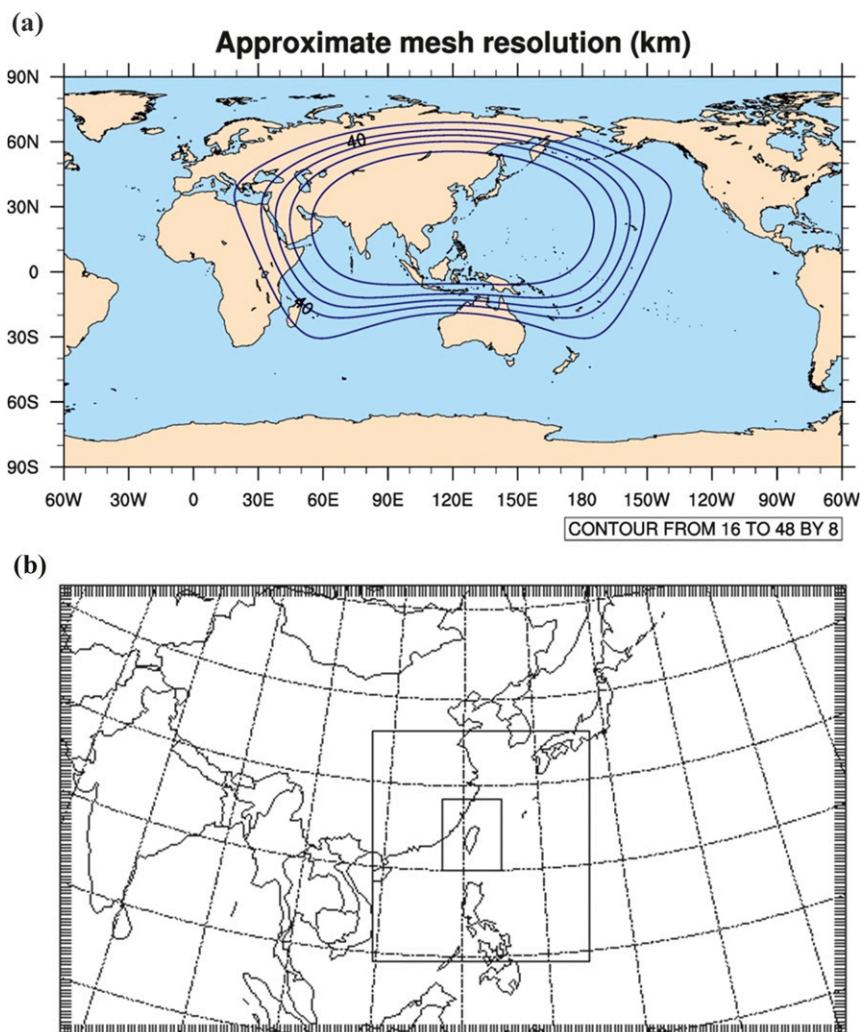


FIG. 1. (a) A variable-resolution mesh with approximately 60-km cell spacing over the globe and a 15-km refinement centered over Taiwan, and (b) the triple-nested domains used in the WRF simulation with 45-, 15-, and 5-km grid cell spacing, respectively.

low pressure was embedded in the monsoon trough near the southeastern coast of China at 0000 UTC 7 August, which consisted of Typhoon Morakot and Tropical Storm Goni (see Huang et al. 2011). With the enhanced monsoon trough, Morakot turned northward across the

CMR on 8 August. During the long residence in the vicinity of Taiwan, Morakot produced a tremendous amount of rainfall over the island, especially in the southern portion. There existed strong southwesterly flow associated with Morakot that brought copious

TABLE 1. Description of model experiments for Typhoon Morakot (2009).

Expt	Description
WRF-15km	WRF simulation with two nested domains (45 and 15 km)
WRF-5km	WRF simulation with three nested domains (45, 15, and 5 km)
CTL	MPAS control run with the unfiltered initial fields
no_SYN	As in CTL, but without the synoptic-scale mode initial fields
no_QBW	As in CTL, but without the QBW mode
no_MJO	As in CTL, but without the MJO mode
MJO+50%	As in CTL, but the intensity of the MJO mode increases by 50%
MJO-50%	As in CTL, but the intensity of the MJO mode decreases by 50%

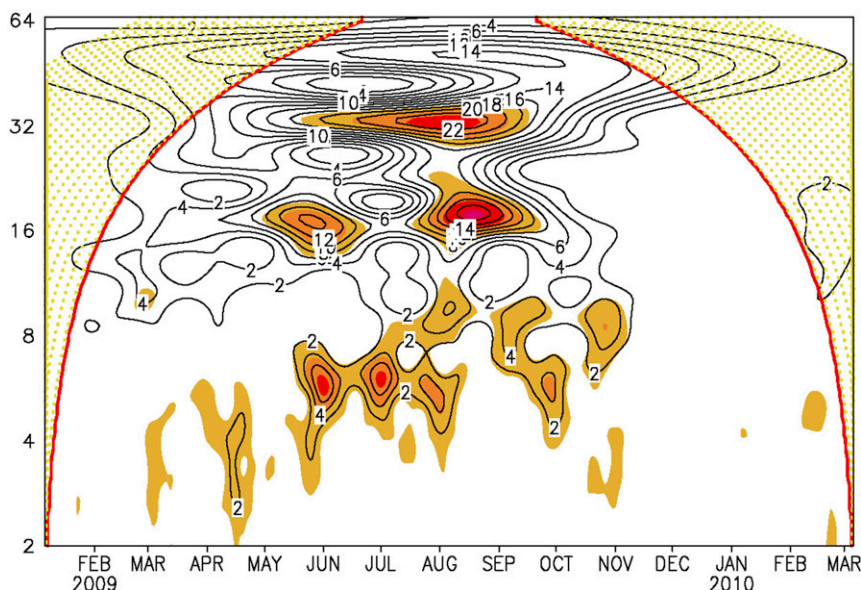


FIG. 2. The wavelet power spectrum (contours in units of $W^2 m^{-4}$) of normalized OLR in the vicinity of Taiwan with shaded red color for confidence levels over 95%. The regions of red dots bounded by two red lines indicate the cone of influence in the wavelet analysis, where edge effects become important.

amounts of moisture from the South China Sea into southern Taiwan and resulted in the heavy rainfall (e.g., Huang et al. 2011; Fang et al. 2011; Wang et al. 2012).

b. The large-scale flow associated with Typhoon Morakot

As mentioned before, previous studies have illustrated that multiscale environmental flows may affect the evolution of Morakot. To identify the active periods for these large-scale flow modes, the power wavelet spectrum of averaged outgoing longwave radiation (OLR) in the vicinity of Taiwan (17° – 30° N, 112° – 130° E) is calculated. The OLR data used in this study are on $1^{\circ} \times 1^{\circ}$ for a period of 425 days.

As shown in Fig. 2, the wavelet analysis of the OLR around August 2009 indicates that there are three significant components with periods of 2–10, 10–20, and 20–60 days, respectively. The first component with a shortest period is the synoptic-scale variation, while the latter two modes with longer periods are referred to as QBW oscillation and MJO oscillation, respectively. Note that the region of red dots in Fig. 2 indicates the “cone of influence” in the power spectrum, where edge effects become important due to the limited length of analysis (Torrence and Compo 1998). Near August 2009, the three major modes are not close to the edge effects.

To examine the influence of the environmental flow at different time scales on Morakot, a Lanczos filter (Duchon 1979) was applied to filter out the component

of the prognostic variables (wind, temperature, moisture, and geopotential height) at the specific time scale. This filter has also been utilized in other studies to provide different modes for analysis (e.g., Liang et al. 2011; Bi et al. 2015). Hong et al. (2010) applied to the wavelet method (also a temporal filter) to obtain the ISO mode for the Morakot event, which appears to be similar to that from the Lanczos filter. The Lanczos filter is applied to grid points, but it should be appreciated that even at longer time scales the spatial structure of MJO may not be well represented. An alternative method widely used for MJO is using empirical orthogonal function (EOF) analysis to obtain the leading principal components (e.g., Wheeler and Hendon 2004; Li and Zhou 2013; Ling et al. 2016). For comparisons with the regional model studies, however, this study applied the Lanczos filter. As indicated in Fig. 2, we decompose the total flow in a long time series into the synoptic-scale SYN mode (with 10-day high pass), the QBW mode (with 10–20-day bandpass), and the MJO mode (with 20–60-day bandpass).

Figure 3 depicts the total and the three corresponding components of the wind fields at 850 hPa at 0000 UTC 6 August 2009. The SYN and QBW modes are in good agreement with Liang et al. (2011) using the National Centers for Environmental Prediction (NCEP) Final (FNL) Operational Global Analysis data. For the SYN mode, there are two anticyclones located to the east and west of Morakot with strong southerly and northerly flows, respectively (Fig. 3b). For the QBW

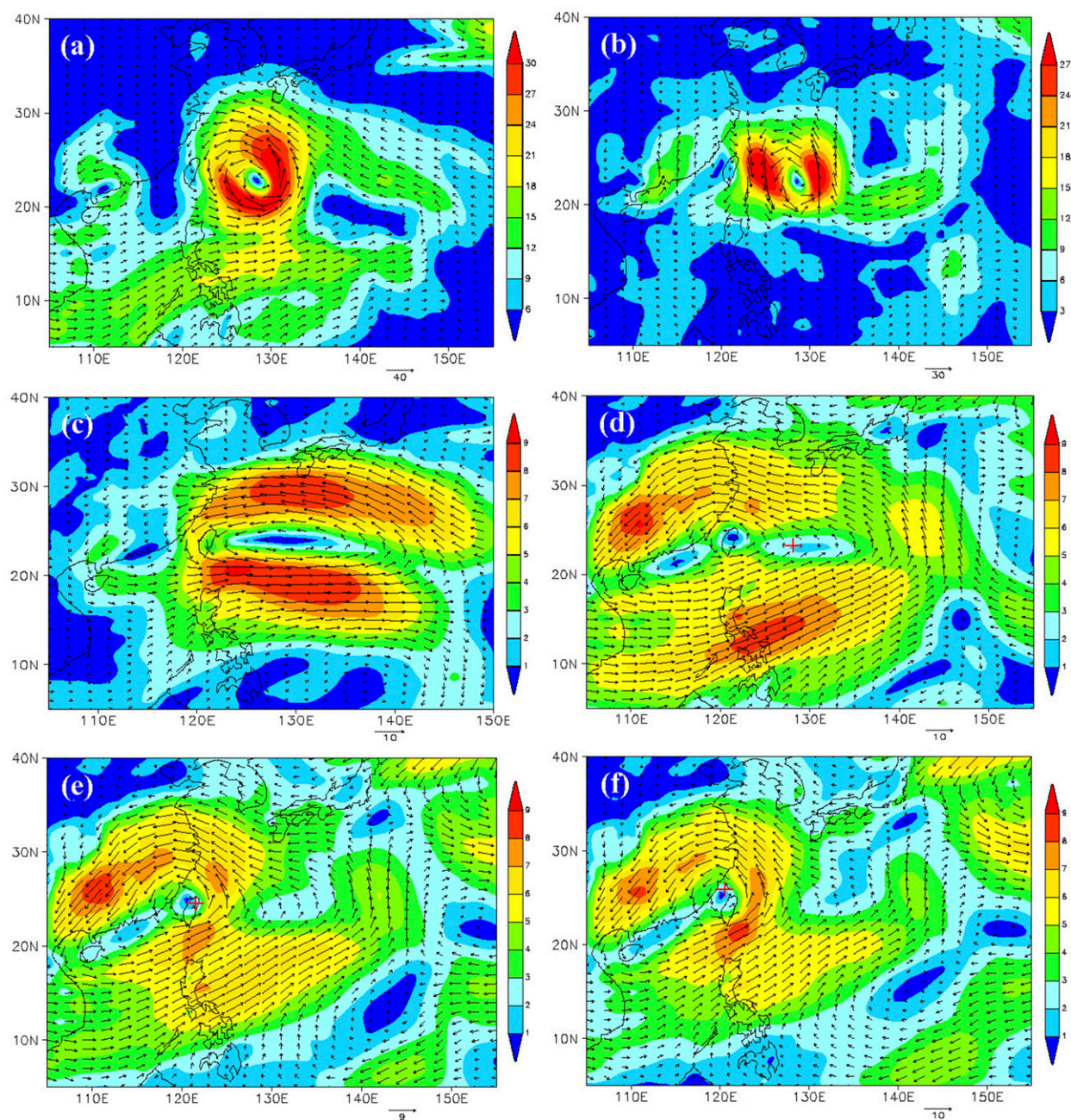


FIG. 3. (a) The unfiltered initial wind field at 850 hPa at 0000 UTC 6 Aug 2009 and the corresponding components on the (b) synoptic scale, (c) QBW scale, and (d) MJO scale. (e), (f) As in (d), but at 0000 UTC 8 Aug and 0000 UTC 9 Aug 2009, respectively. The red plus signs in (e) and (f) denote the center of Typhoon Morakot.

mode, a cyclonic gyre of low-frequency flow was embedded in a large monsoon gyre (Lander 1994) (Fig. 3c). The time evolution of the MJO mode is shown in Figs. 3d–f. The major features of the MJO mode obtained by the Lanczos filter correspond well to phase 7 categorized by the EOF composite of Wheeler and Hendon (2004). The cyclonic circulation of the MJO mode extends northward above 35°N (Fig. 3d) in

association with a typical monsoon gyre around Taiwan, which has also been shown in Hong et al. (2010) and Liang et al. (2011). The center of the monsoon gyre was located near central Taiwan at 0000 UTC 6 August when Morakot was embedded in the eastern flank of the monsoon trough that extended to about 145°E. Morakot moved westward toward the center of the monsoon gyre in the subsequent days. After making landfall at eastern

Taiwan, Morakot crossed the CMR and then coalesced with the monsoon gyre at 0000 UTC 8 August. Later on, both Morakot and the monsoon gyre moved together toward the northwest. The above analysis suggests strong interactions between Morakot and the MJO mode. The influences of the monsoonal flow on the track evolution of Morakot will be investigated in the next section.

c. Sensitivity experiments

In addition to the control experiment (CTL), several sensitivity experiments described in Table 1 are conducted for exploring the influence of different time-scale large-scale flows on Typhoon Morakot. In the first three sensitivity experiments, the SYN, QBW, and MJO components are filtered out from the model initial fields, denoted by no_SYN, no_QBW, and no_MJO, respectively. The last two experiments, MJO−50% and MJO+50% with 50% decreased and increased magnitude of the MJO intensity in the initial field, respectively, are used to investigate the impacts of the large-scale flow variation on the track evolution of Typhoon Morakot. Note that MJO+50% is used to illustrate the impact of the enhanced MJO intensity and does not represent the actual variability in a climatological sense. As seen in Fig. 3d, the increase in the MJO by 50% will correspond to an increase in the wind speed at a magnitude of about $1\text{--}4\text{ m s}^{-1}$.

4. Results for Typhoon Morakot

a. Track and rainfall simulations

Figure 4a shows the best track from the Central Weather Bureau (CWB) of Taiwan and the simulated tracks for MPAS and WRF forecasts from 0000 UTC 6 August to 1200 UTC 9 August 2009. The MPAS simulation from the control experiment (with the unfiltered initial fields) captures the movement of Morakot in better agreement with the best track as compared with the WRF simulations with 15- or 5-km resolution. Note that both MPAS and WRF simulations use the same physical schemes. The simulated typhoon by MPAS moves westward at the early stage, makes landfall close to the observed position, and then translates northwestward or northward, while the two simulated tracks by WRF appear to deviate somewhat southward before landfall and considerably westward after landfall. Without initial vortex bogussing, the simulated intensities of Morakot before landfall for both MPAS and WRF are considerably weaker than the observed (Fig. 4b). The simulated Morakot gradually develops within one day and reaches its peak intensity around 1200 UTC 7 August 2009, and then slightly weakens after landfall. The simulated intensity of Morakot after landfall for both models is in good agreement with the observation.

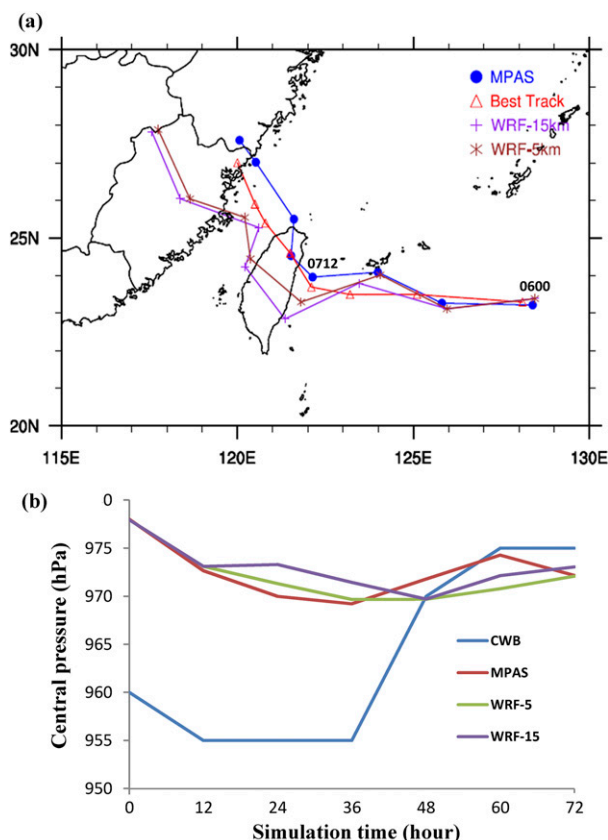


FIG. 4. (a) The best track of Morakot from CWB (red) and the simulated tracks from the experiments MPAS, WRF-15km, and WRF-5km, valid from 0000 UTC 6 Aug to 1200 UTC 9 Aug 2009 at an interval of 12 h. (b) The 84-h evolution of the simulated sea surface central pressure starting from 0000 UTC 6 Aug 2009 for the MPAS, WRF-15km, and WRF-5km experiments, and the CWB observations at a 12-h interval.

With the reasonably simulated track and intensity, the simulated 72-h rainfall for MPAS is also in good agreement with the observation, despite the fact that the observed maximum rainfall (about 2400 mm) over the southern CMR is somewhat underpredicted by MPAS with a value of about 1800 mm, which lies in between the WRF-5km value (about 2000 mm) and the WRF-15km value (about 1600 mm) (Fig. 5). Note that the simulated tracks of Morakot shift farther southward in both WRF-15km and WRF-5km than that in MPAS during 7 August. As a result, the WRF simulations overestimate the 24-h rainfall over southern Taiwan, especially near the southern end of the CMR (figures not shown). Tremendous daily rainfall over 1400 mm is produced in central and southern Taiwan as Morakot moves slowly northward away from the island on 8 August, while both the MPAS and WRF forecasts only reach about 1000 mm and fail to predict a sufficient amount of such extreme rainfall possibly due to the

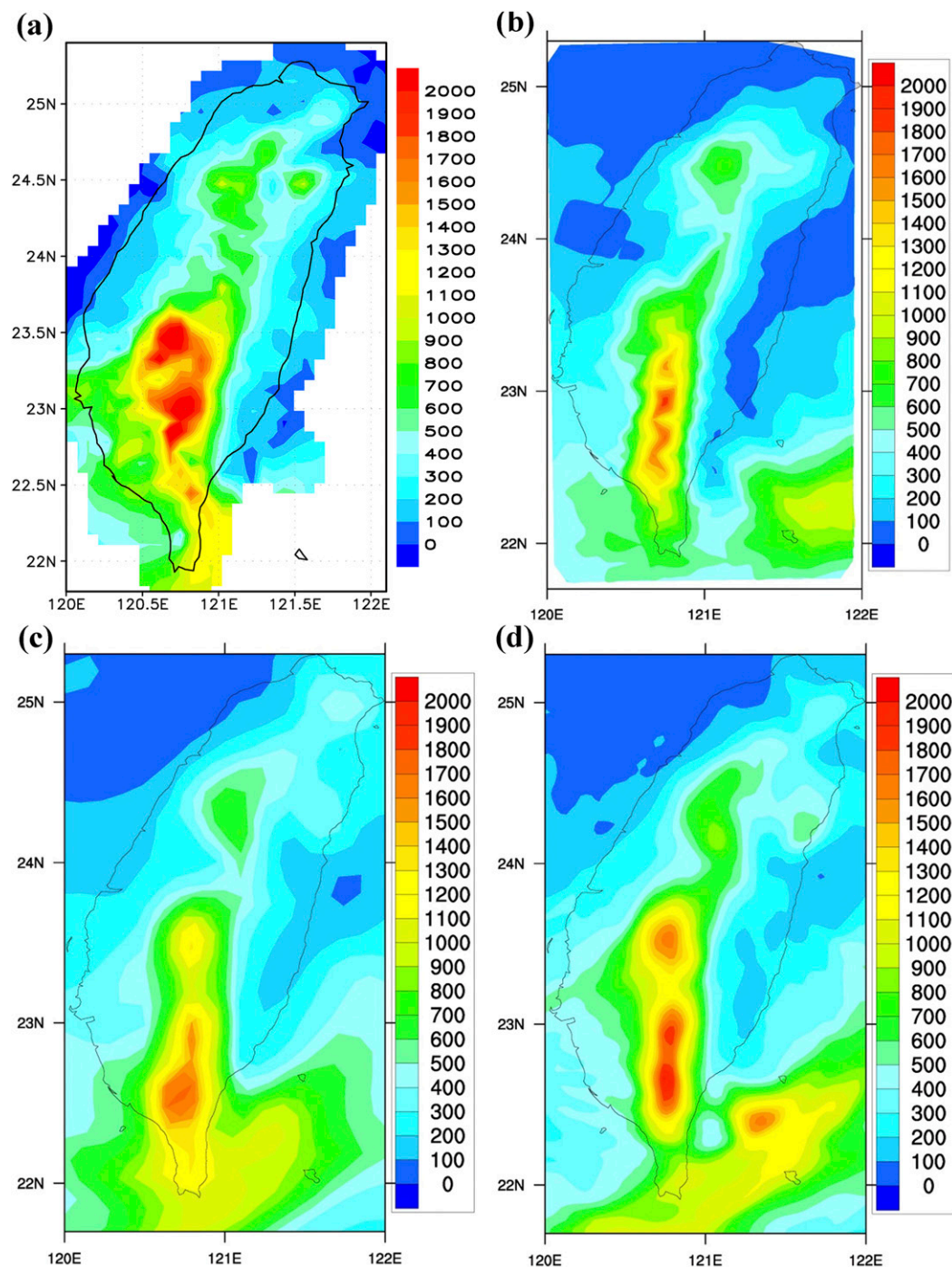


FIG. 5. (a) The observed accumulated rainfall (mm) over three days (0000 UTC 6 Aug–0000 UTC 9 Aug 2009) from CWB, and the corresponding simulated rainfalls from the (b) MPAS, (c) WRF-15km, and (d) WRF-5km experiments. The rainfall is shaded with a maximum of 2000 mm.

coarse resolution and/or physics problems. Nevertheless, the spatial distributions of both simulated rainfalls agree well with the observation, except for the slightly southward displacement of the rainfall maxima.

In general, the current MPAS model with variable resolution (60–15 km) is capable of predicting both the track affected by the CMR and the observed extreme rainfall over southern Taiwan. Thus, we may utilize the

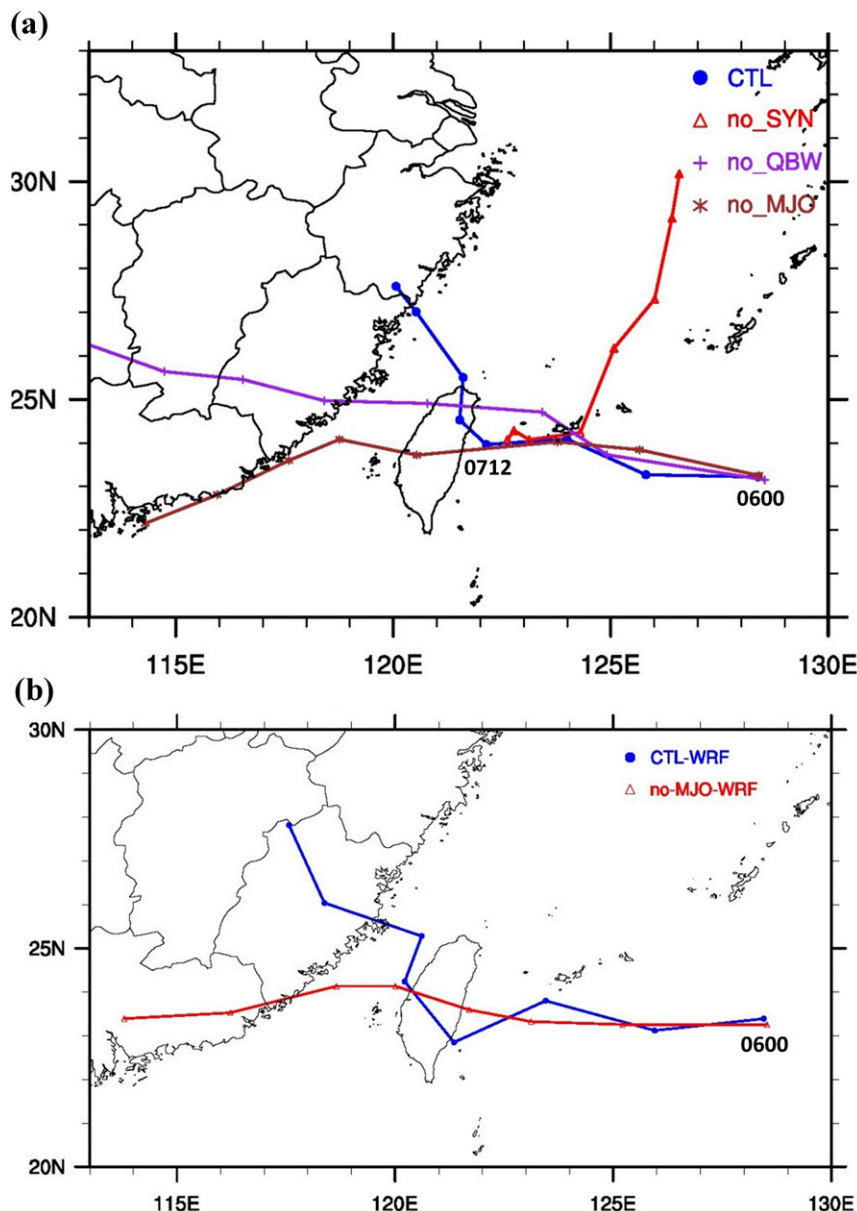


FIG. 6. (a) The simulated Morakot tracks using MPAS for the control experiment CTL and sensitivity experiments no_SYN, no_QBW, and no_MJO valid from 0000 UTC 6 Aug to 1200 UTC 9 Aug 2009. (b) As in (a), but for the experiments CTL (blue) and no_MJO (red) using WRF. The typhoon tracks are marked every 12 h.

MPAS model to explore the impacts of multiscale flow variations on the track evolution of Morakot using sensitivity experiments.

b. The impact of large-scale flow on Morakot's track

The simulated 84-h tracks in CTL, no_SYN, no_QBW, and no_MJO experiments are shown in Fig. 6a. In the absence of synoptic flow, the simulated Morakot tends to divert north-northeastward away earlier, due to the effect of the filtered synoptic steering flow around

Morakot, which agrees with the WRF simulation of Liang et al. (2011). By contrast, Morakot moves too westward when the MJO mode is completely filtered out, so that Morakot directly crosses central Taiwan without the observed northward turning. This result reveals that the interaction between the large-scale monsoon and Typhoon Morakot plays a critical role in the northward turning after landfall. The westward track for no_QBW is similar to that for no_MJO, but it is farther north before and after landfall. Using

a nondivergent barotropic model, Carr and Elsberry (1995) demonstrated that tropical cyclones embedded in a monsoon gyre may make a sudden north turn in the track under the influence of the large-scale southerly steering flow. The simulated results in this study are consistent with their investigation.

The Morakot track without the MJO mode simulated by WRF is shown in Fig. 6b, which appears to be close to the counterpart of MPAS, in particular at the earlier stages before and near landfall at Taiwan. Since both MPAS and WRF use identical initial conditions and physical schemes, the increased difference in both tracks after departure may be caused by the model dynamical core and/or lateral boundary conditions. However, no true state can be used to evaluate which one indeed is more consistent. Nevertheless, the MPAS simulations at 60–15-km variable resolution are justified and can be used for the investigation of the underlying mechanisms responsible for the track evolution.

To examine the role of the MJO variation in affecting the evolution of Morakot, two additional experiments, MJO+50% and MJO−50% are conducted, which enhances and decreases the MJO mode by 50% in the initial condition, respectively. Figure 7 shows the simulated tracks for MJO+50% and MJO−50%. In MJO+50%, Morakot closely follows the CTL track at the early stage but then suddenly turns northward around 1200 UTC 7 August before approaching Taiwan. The track for MJO−50% in general is westward, which is quite similar to that for no_MJO experiment except with a less southward deviation at the later stage after departure from Taiwan. The later migration of the tracks from the no_MJO, MJO−50%, CTL, and MJO+50% experiments suggests an effective role of the MJO in steering Morakot northward.

To understand why Morakot translates in a different path under the influence of MJO with various intensities, the differences between the flows with the modulated MJO and CTL experiments are shown in Fig. 8. For the flow difference at 0600 UTC 7 August between no_MJO and CTL experiments, an anticyclonic vortex at 850 hPa is located to the northeast of Taiwan (figures not shown), which largely results from the different locations of the simulated Morakot's center in the two runs. The southern flank of the anticyclone provides the intense northeasterly wind toward eastern Taiwan. There are broad areas of easterly to northeasterly winds over the western North Pacific, extending from farther east of Taiwan to the South China Sea. At 1200 UTC 7 August, these easterly to northeasterly wind differences over the western North Pacific further increase (Fig. 8a). Larger differences with strong anticyclonic flow are also produced in the vicinity of Goni

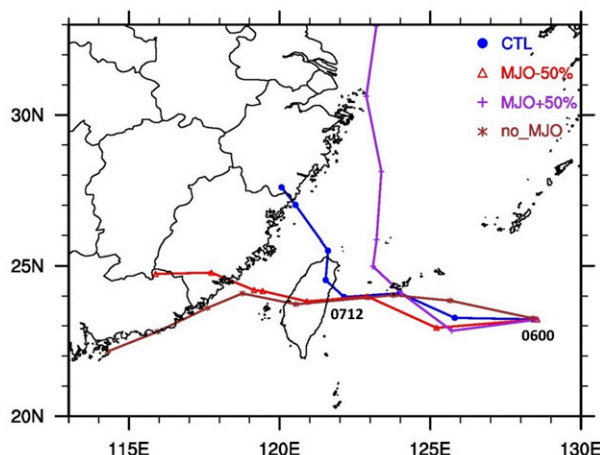


FIG. 7. As in Fig. 6a, but for the experiments CTL, no_MJO, MJO−50%, and MJO+50%.

cyclone near (20°N, 108°E), indicating that Goni indeed significantly weakens in the absence of the MJO mode. The development of the initial MJO component at later times leads to the increased westerly to southwesterly wind to the south of Typhoon Morakot. Consequently, Morakot takes a westward track across central Taiwan without a northwest to north turn when the MJO mode is removed.

In contrast, the southerly to southwesterly winds in the vicinity of Morakot have been considerably enhanced at 0000 UTC 7 August when the initial MJO intensity is increased by 50% (not shown). At 0600 UTC 7 August, these southerly wind components develop farther east of Taiwan, providing stronger asymmetric southerly to southwesterly flows southeast of the typhoon center (Fig. 8b). This may explain why the simulated Morakot takes an earlier north turn under the stronger MJO condition. For the CTL experiment (with the intact MJO intensity), the simulated Morakot develops in between MJO+50% and MJO−50% as seen in Fig. 7. The northward turn of Morakot after landfall takes place around the time when it begins to coalesce with the monsoon gyre (Fig. 3).

c. Diagnostics of vorticity tendency budget

The wind increments in Fig. 8 provide favorable large-scale conditions that are helpful to explain the track evolution. Analyses of vorticity budget may help us understand the vortex movement in response to large-scale flow variations (e.g., Holland 1983). The vorticity budget terms described in the vorticity equation of appendix A are calculated on the height coordinate with a constant spacing of 200 m as interpolated from the hybrid coordinate. We found that the simulated Morakot is weaker for no_MJO and develops a vortex only with a

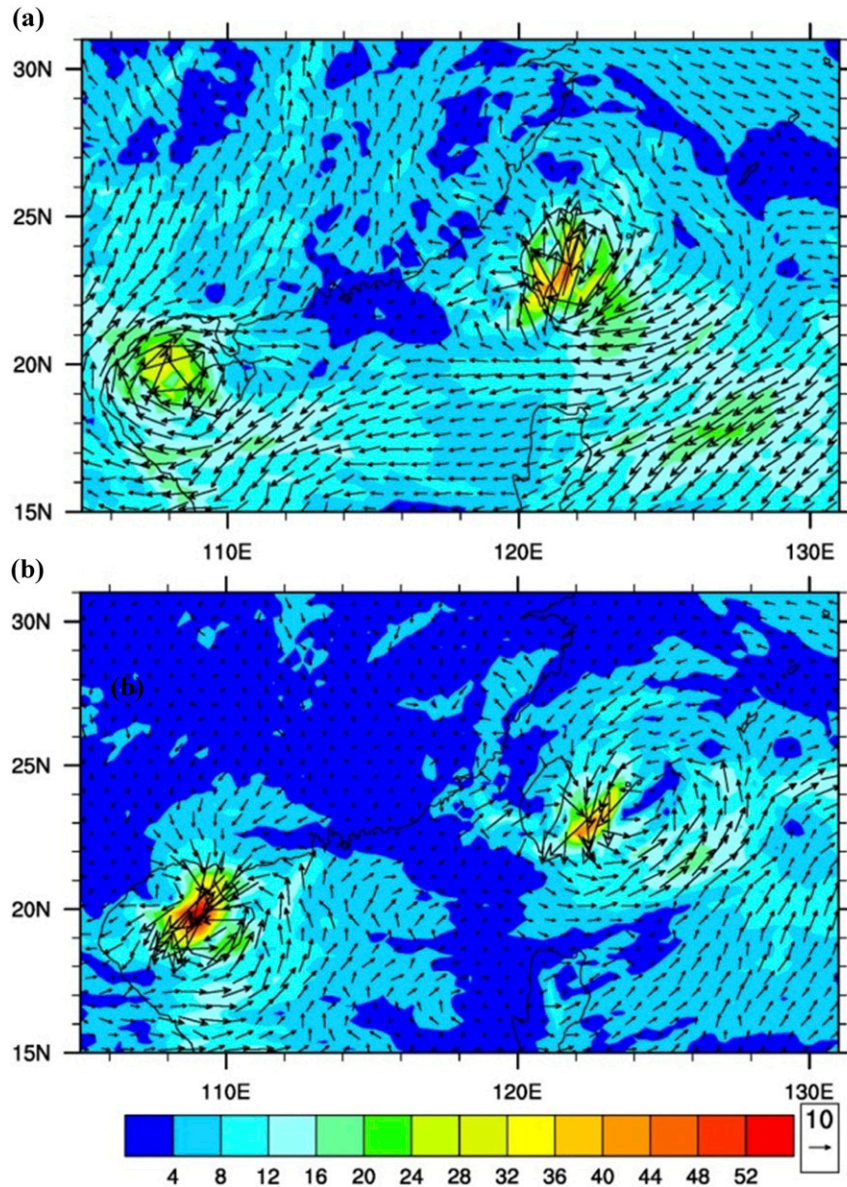


FIG. 8. The differences in 850-hPa wind vectors and their magnitudes (contours shaded in m s^{-1}) at (a) 1200 UTC 7 Aug 2009 between no_MJO and CTL and (b) 0600 UTC 7 Aug 2009 between MJO+50% and CTL.

shallow upright structure below 6–7-km height. Thus, we adopt the averaged results in the layer between 3–5-km height since the CMR as resolved by the model is at a maximum height of about 2.8 km. The sequential vorticity budget terms over 5 min (i.e., six time steps) are also averaged for temporal smoothing.

Figure 9 shows the averaged vorticity tendency and horizontal wind at 3-km height as well as vorticity budget terms associated with the simulated Morakot at 1200 UTC 7 August 2009 for CTL. In this layer (3–5-km heights), the contribution of boundary layer turbulent

diffusion (mostly in the lower 1–2 km) is small and thus is not included. The vorticity budget terms (see appendix A) are summed and compared with the vorticity tendency (Figs. 9a,b). Both quantities agree well with each other in terms of geometric distributions, indicating that the inherent numerical smoothing in MPAS (not accounted for in the vorticity budget) is not physically dominant. However, both also indicate that alternating positive and negative contributions are induced around the outer vortex so that the ensuing vortex movement is not clearly revealed. The vortex actually

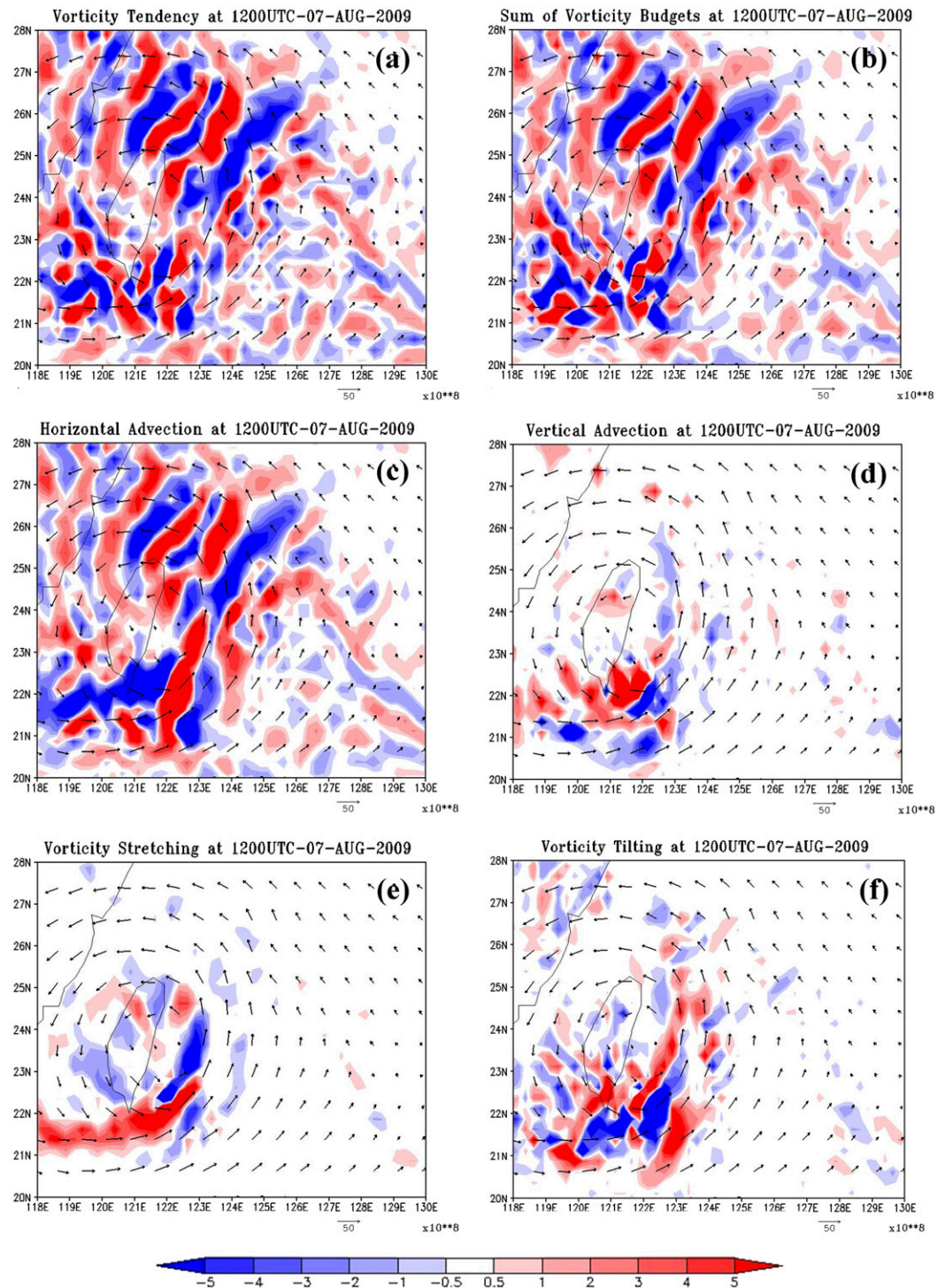


FIG. 9. (a) The vorticity tendency averaged over the 3–5-km layer in height, and horizontal wind (m s^{-1}) at 3-km height associated with the simulated Morakot vortex at 1200 UTC 7 Aug 2009 for CTL. (b)–(f) As in (a), but for (b) sum of the budget terms, (c) horizontal advection, (d) vertical advection, (e) vorticity stretching, and (f) vorticity tilting (units of s^{-2} after multiplied by 10^8).

moves northwestward at this time, which is consistent with the presence of several banded regions with large positive vorticity tendency just north of the vortex center.

This positive vorticity tendency away from the mountain appears to be dominated by horizontal vorticity advection (Fig. 9c) that resembles the vorticity tendency. Vertical advection (Fig. 9d) only has the positive contributions in the region of intense upward motions south of Taiwan. Similar to vertical advection, vertical stretching also exhibits positive contributions near the same region (Fig. 9e). As the vortex moves northward at a later time, these intense upward motions shift northward over the southwestern coast of Taiwan and CMR (figures not shown) and the associated heavy rainfall produces strong latent heating that may retard the northward departure of the vortex (e.g., Chien and Kuo 2011; Wang et al. 2012). Positive vorticity tendency may also be produced by vorticity tilting in the inner regions of the vortex core (Fig. 9f). However, it should be noted that the large negative zone, aligned roughly west–eastward south of the vortex center, may equivalently contribute to a large wavenumber-1 northward movement as shown later. Solenoidal effects (not shown) are much smaller as compared to the other physical processes.

For comparison with CTL, Fig. 10 shows the averaged vorticity budget and the vortex circulation at 3-km height at 0600 UTC 7 August for no_MJO. Similar to CTL, the total vorticity budget (Fig. 10b) generally agrees well with the vorticity tendency (Fig. 10a) in terms of spatial distributions. Again, the vorticity tendency in the outer vortex is dominated by the horizontal advection of absolute vorticity (Fig. 10c). Positive contributions from vertical advection are mainly induced near and over southern Taiwan (Fig. 10d). On the layer average, vorticity stretching gives the large positive contributions induced somewhat southward of the stronger upward motions (Fig. 10e). The negative effects of vertical stretching offshore and near the southwestern coast result from horizontal divergence (not shown) where the northerly flow is accelerating southward in association with decreased upward motions with height. Vorticity tilting exhibits more localized structures with major positive effects in the stronger northerly flow offshore of western Taiwan (Fig. 10f). Comparing the results of the vorticity tendency for CTL and no_MJO (Fig. 9a vs Fig. 10a), the latter gives comparable positive contributions to the north and south of the vortex center so that the vortex does not show a preference in southward or northward movement. For CTL, the dominant positive contributions to the north rather than the south of the vortex center may be attributed to the induced horizontal advection by the stronger southerly and cyclonic flow to the east and northeast of the vortex center that transports

stronger positive vorticity northward (see Fig. 9a). The horizontal vorticity advection becomes more dominant at 1800 UTC 7 August (not shown) as Morakot after landfall is making a northward to northwestward turning. To quantify the contributions from different physical processes to the typhoon translation before and after turning, wavenumber-1 diagnostics of typhoon circulation and vorticity dynamics will be presented in section 6.

5. Results for Typhoon Megi

a. Megi and the associated large-scale flow

Megi formed as a tropical disturbance east-southeast of Guam on 10 October 2010, began to significantly develop on 12 October, and then intensified into a tropical storm [hereafter named by the Japan Meteorological Agency (JMA)] around 1200 UTC 13 October. In the following days, Megi continued to intensify while moving toward the Philippines. On 15 October, it was upgraded to a typhoon by JMA. It then began to quickly deepen with a well-defined eye apparent on 16 October. Megi reached its peak intensity of superintense typhoon with a minimum central pressure of 895 hPa early on 17 October. Megi made landfall at the northeastern Philippines on 18 October 2010, considerably weakened after passing over the northern Philippines, and then reintensified when moved into the South China Sea before taking a rapid north turn on 19 October. More detailed information about the evolution of Megi has been given by Bi et al. (2015) and Chen and Wu (2016).

The monsoonal flow can be divided into two components, a quasi-biweekly oscillation (QBW) and a 20–60-day oscillation (MJO). A 10–60-day filtered flow is applied by Bi et al. (2015) for ISO to isolate the impact of the monsoon gyre, which is equivalent to a combination of our QBW and MJO for Morakot. To compare with our analysis of Morakot, we focus on the 20–60-day MJO mode.

Figure 11 shows the initial unfiltered flow and evolution of the associated MJO at 850 hPa during the active period of Megi (0000 UTC 17 October–0000 UTC 21 October). There existed a quasi-stationary cyclonic circulation over the South China Sea from 17 to 22 October, as a typical flow pattern of the MJO mode. Typhoon Megi was located on the eastern flank of this low pressure system at its early stage and then moved westward toward the monsoon gyre. On 20 October 2010, both the typhoon center and the monsoon gyre coalesced and then moved northward together in the subsequent days (Bi et al. 2015).

b. The experimental setup

To investigate the impact of the MJO mode on the track evolution of Megi, we conduct two MJO sensitivity experiments: no_MJO (without the MJO mode) and

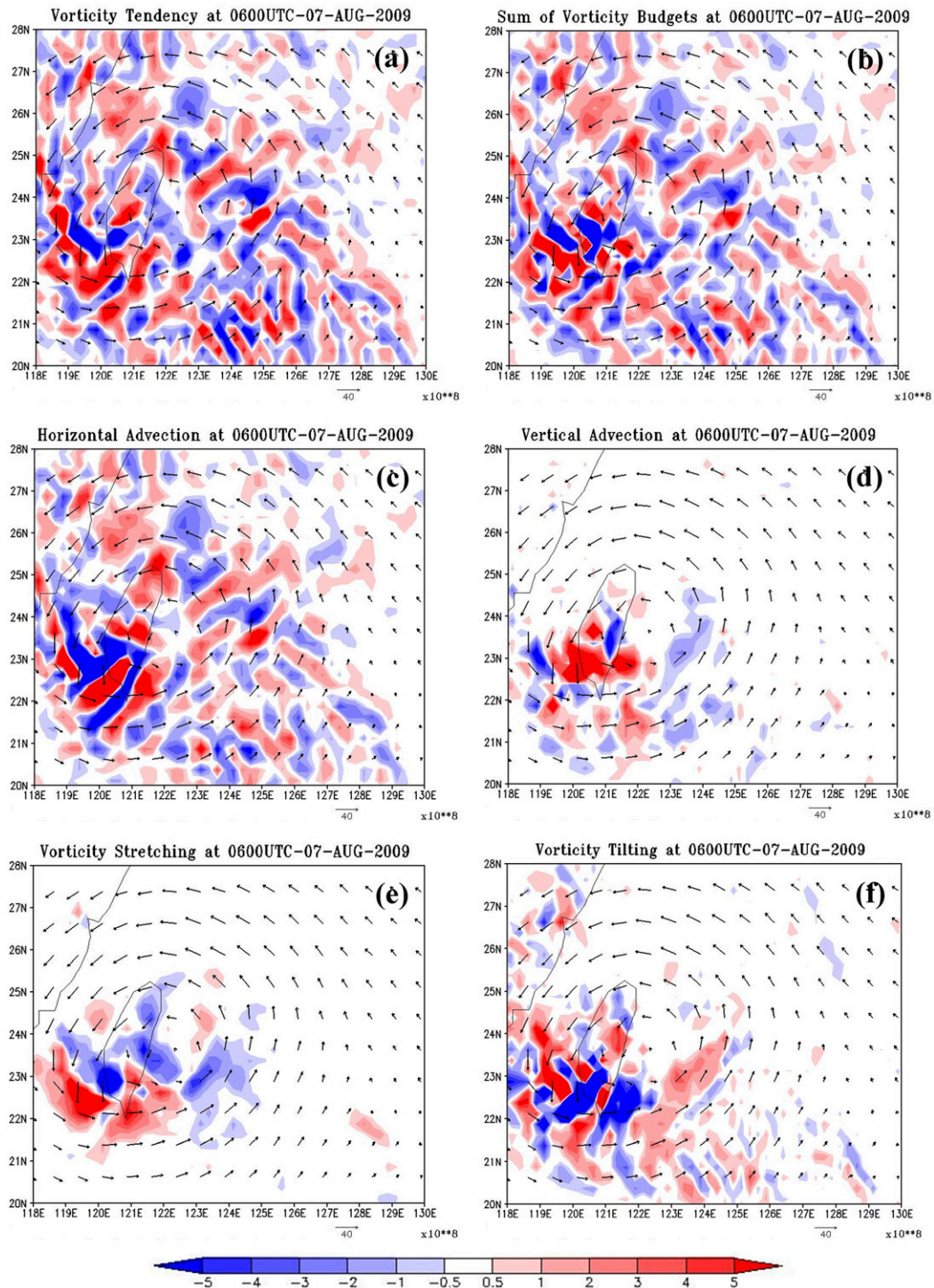


FIG. 10. As in Fig. 9, but at 0600 UTC 7 Aug 2009 for no_MJO.

MJO+50% (with the extra 50% MJO mode). In the control experiment (with the unfiltered total flow), the NCEP FNL data on $1^\circ \times 1^\circ$ grids are used as the model initial condition. We used the NCEP FNL data for Megi

rather than the ERA-Interim for the same reason explained by Bi et al. (2015) that the latter fails to capture the turning track of Megi. The numerical simulation starts at 0000 UTC 17 October 2010 and is integrated for

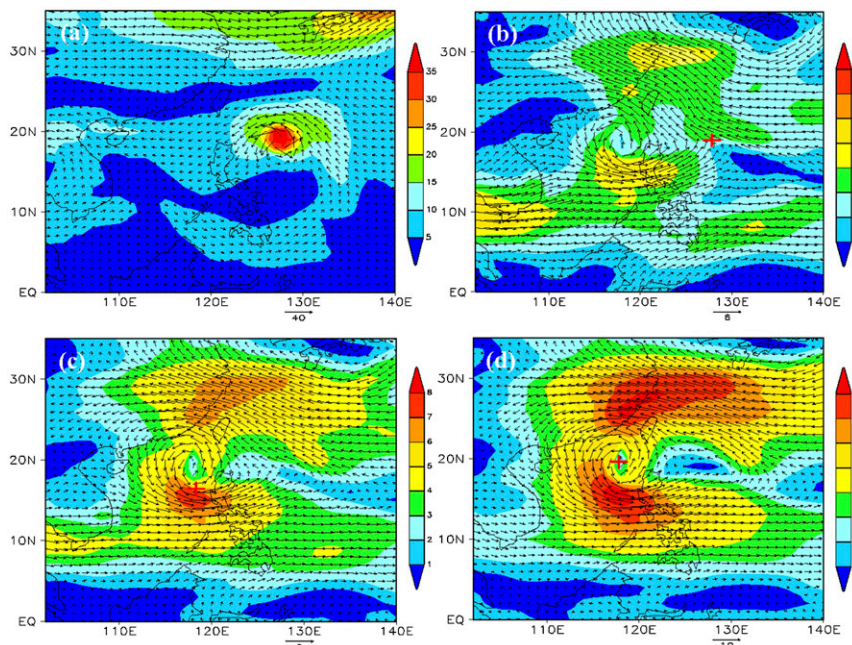


FIG. 11. (a) The initial wind field at 850 hPa at 0000 UTC 17 Oct 2010, and the 20–60-day bandpass-filtered wind field (MJO) at 850 hPa at (b) 0000 UTC 17 Oct, (c) 0000 UTC 19 Oct, and (d) 0000 UTC 21 Oct 2010. The red plus sign in (d) indicates the center of Megi.

136 h, covering the period during which Megi makes landfall on the Philippines and later takes a north turn after departure. All the simulations for Megi have used the same physical schemes as in the Morakot simulations.

c. Simulated track and steering flow

Figure 12 shows the best track of JMA and the simulated tracks for CTL and no_MJO and MJO+50%. In the control experiment (CTL), the simulated track follows the best track very well with nearly the same northward turning (around 1800 UTC 19 October), while somewhat faster as it nears southeastern China. In the no_MJO experiment, Megi deviates southward at the early stage. After crossing the northern Philippines, Megi continues to move westward without an abrupt north turn. A similar westward movement without the northward turn west of the northern Philippines is also exhibited in the experiment without the ISO in Bi et al. (2015). Comparing both tracks, we find that the extra QBW mode leads to a less northward movement at later stages, thus making landfall at Hainan Island. The results indicate that the monsoonal flow plays a crucial role in the northward movement, which has also been demonstrated in the Morakot experiments.

To understand why Megi moves in different tracks in the absence and presence of the MJO mode, the steering flow is examined at two times (1200 UTC 19 October near turning and 0000 UTC 20 October after turning) as

shown in Fig. 13. Before the turning, the simulated Megi circulations with and without the MJO mode are at distant regions so that their wind differences are less useful for explaining the flow steering as for Morakot. Instead, the zonal (U) and meridional (V) wind components of the flow are averaged in a square area centered at the typhoon center. As seen, the average flow below the midtroposphere is not sensitive to the area size of average, owing to that the storm is more intense and symmetric in the lower troposphere. The vertical

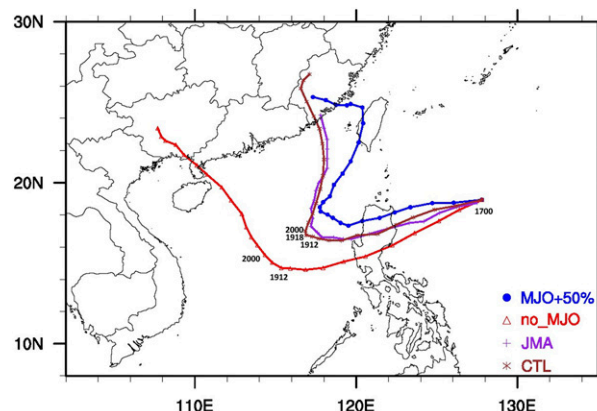


FIG. 12. The best track of Megi from JMA (purple) and the simulated tracks for control (brown), no_MJO (red), and MJO+50% (blue) from 0000 UTC 17 Oct to 1200 UTC 23 Oct 2010 at an interval of 6 h.

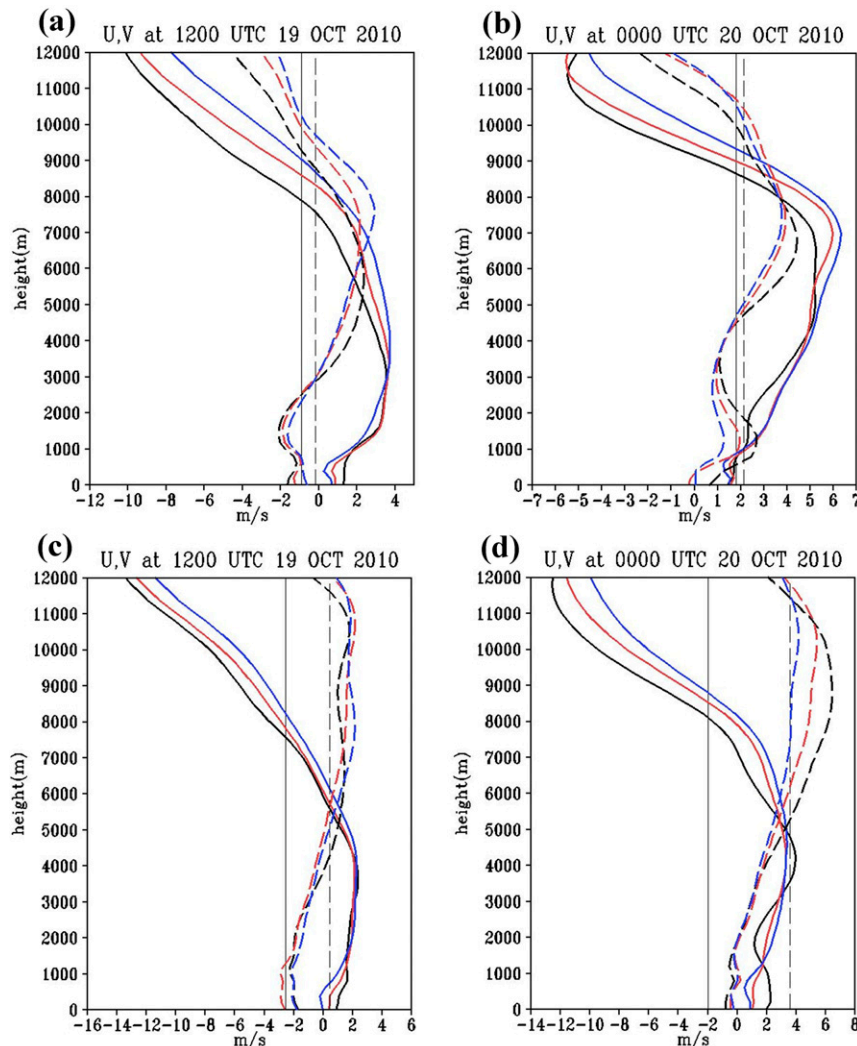


FIG. 13. Vertical variations of the averaged zonal (solid) and meridional (dashed) wind components in bold lines for (a) CTL at 1200 UTC 19 Oct 2010 and (b) CTL at 0000 UTC 20 Oct 2010. (c),(d) As in (a),(b), but for no_MJO from the simulated Megi. Wind components are averaged in the box of the Megi center at $8^{\circ} \times 8^{\circ}$ (black), $12^{\circ} \times 12^{\circ}$ (red), and $16^{\circ} \times 16^{\circ}$ (blue). The thin solid (dashed) vertical line indicates the vertical average of the $8^{\circ} \times 8^{\circ}$ average zonal (meridional) wind over 1–12-km height.

mean (averaged over 1–12-km height) of U and V in the square ($8^{\circ} \times 8^{\circ}$) is also calculated to give a reference for steering. A radius of 5° – 7° and a depth of 850–300 hPa are normally applicable for average of reanalysis data (e.g., Carr and Elsberry 1990), but there is no optimal way to determine the actual steering for high-resolution simulations. For CTL, the vertical mean of the averaged flow in $8^{\circ} \times 8^{\circ}$ exhibits a small negative U and a nearly zero value of V at 1200 UTC 19 October, which is consistent with the actual slow westward movement of Megi at this time. After turning northward at 1200 UTC 19 October, Megi slowly moves northeastward and is associated with upward increased U and V at 2000 UTC

20 October. As seen in Fig. 11c, the large-scale westerly flow of the MJO mode just west of the northern Philippines is increasing with time. It appears that the increased westerly flow, originating from the monsoon gyre, resists the westward movement of Megi when it moves into this flow regime. The averaged V velocity is generally northward in the troposphere as to induce the northward movement of Megi after turning. Similar to Morakot, northward turning occurs when the center of Megi is going to coalesce with the monsoon gyre, as also shown in Bi et al. (2015).

When the MJO mode is filtered out from CTL, the averaged U becomes mostly negative (i.e., westward) in

association with very small positive V at 1200 UTC 19 October, regardless of the average size (Fig. 13c). Note that the average region for no_MJO is located about 500 km southwest of the turning point of the CTL track. In the absence of the MJO, the westward movement of Megi is consistent with the prevalence of westerly flow west of the Philippines exhibited by the MJO mode. Indeed, Megi's westward propagation is faster for no_MJO than for CTL, possibly due to the effect of the stronger westward steering flow (larger negative U) above 7-km height (Fig. 13d). The meridional V also increases upward 12 h later (0000 UTC 20 October) and its vertical mean is considerably larger than in CTL, resulting in a faster northward movement as seen in Fig. 12. As indicated in Figs. 11c and 11d, Megi is situated in a pathway along the cyclonic flow of the monsoon gyre west of the northern Philippines, and that is why Megi is steered favorably toward the northwest at later stages in the absence of the MJO mode.

d. Diagnostics of vorticity tendency budget

The vorticity tendency budget is also diagnosed for Megi to understand the physical processes involved in the vortex evolution. Since the vertical structure of the intense Megi is upright up to 12 km in height, vorticity budget terms are averaged from 1- to 8-km height. Figure 14 shows several major vorticity budget terms and the associated typhoon circulation at 1200 UTC 19 October (when Megi is about to take a north turn) and at 0000 UTC 20 October (when Megi just completes the north turn) (see Fig. 12) for CTL. During the off-shore movement off the northern Philippines, Megi has redeveloped to a supertyphoon with a maximum wind speed over 80 ms^{-1} and an updraft intensity over 4.5 ms^{-1} , which are much stronger than Morakot. At 1200 UTC 19 October, the sum of all the vorticity budget terms (Fig. 14a) resembles the horizontal advection (Fig. 14c), and their positive contributions with a structure of quartic bands weigh more to the west of the vortex center than to the east. Vertical advection exhibits quite symmetric tendency around the vortex and thus will not induce a preferable moving direction. Vorticity tilting has considerable positive and negative contributions to the west and east, respectively, of the inner vortex with similar distributions of stronger upward motion (not shown). Hence, these two terms do not greatly influence the northward vortex movement. Vorticity stretching, however, appears to have large positive and negative impacts to the south and north, respectively, of the center before the north turn (Fig. 14e). A positive contribution also appears to the northwestern flank of the inner core. As will be shown

later, the vorticity stretching indeed contributes to a northwestward vortex translation. After the vortex makes the north turn at 0000 UTC 20 October, the horizontal advection (and thus total vorticity budget) contributes positively to the north and east of the center showing a pattern of quintic bands (Figs. 14b,d). For vorticity stretching, the previous larger positive weighting now becomes more circular around the vortex except to the northeast of the vortex center (Fig. 14f). A close look at the induced negative tendency indicates that its distribution is more circular around the vortex center. Consequently, the vortex translation is west-southwestward, corresponding to the positive vorticity stretching. This will be better envisioned by the wavenumber-1 decomposition in section 6.

As the MJO mode is filtered out, Megi moves west-southwestward at the earlier stages and is going to take a northwest turn at 1200 UTC 19 October as shown in Fig. 12. Figure 15 shows the major vorticity budget terms (averaged in 1–8-km height) and the vortex circulation at 3-km height at this time. As seen, the vortex structure is highly symmetric with flow intensity over 80 ms^{-1} . Both the net vorticity tendency and horizontal advection well resemble each other, showing a pattern of quartic bands with larger positive contributions (Figs. 15a,b). Similarly, vertical advection is important only within the inner core of the vortex (Fig. 15c), while vorticity stretching also has larger positive contributions to the south and west of the center (Fig. 15d). Vorticity tilting mainly contributes to the west of the center and thus favors a westward movement (not shown).

For both CTL and no_MJO, vertical advection and vorticity tilting play a much less important role in the northward translation of Megi compared to Morakot. We will conduct wavenumber decompositions of the typhoon circulation and vorticity budget for both typhoons to highlight contributions from different physical processes and their important differences in the next section.

6. Comparison of vortex evolution between Morakot and Megi

Diagnosis of asymmetric components may help us to understand the movement of a vortex (e.g., Wu and Wang 2000). In this section, we examine wavenumber-1 diagnostics of the vorticity dynamics and apply the regression of the vorticity tendency budget (see appendix B) to quantify the relative contributions of different physical processes involved in the vorticity equation. For both typhoons, the typhoon center is defined as the position of the weakest wind in the vortex core. A bicubic interpolation is employed to find the position of

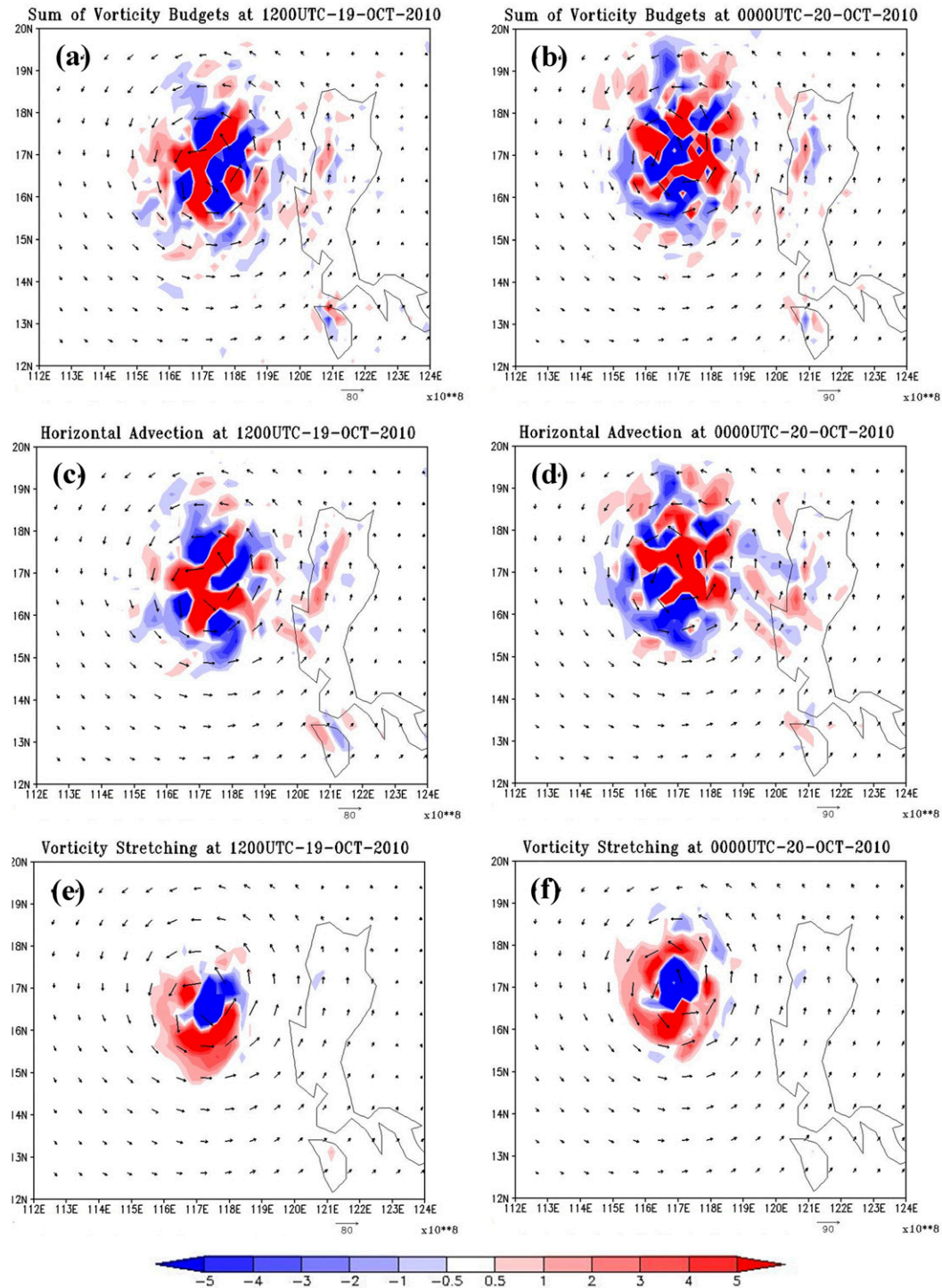


FIG. 14. (a),(b) Sum of the budget terms in the vorticity equation averaged over 1–8-km height, and horizontal wind (m s^{-1}) at 3-km height, from the CTL simulation of Megi at (a) 1200 UTC 19 Oct 2010 and (b) 0000 UTC 20 Oct 2010. For these two times, (c),(d) horizontal vorticity advection is plotted and (e),(f) vorticity stretching is given.

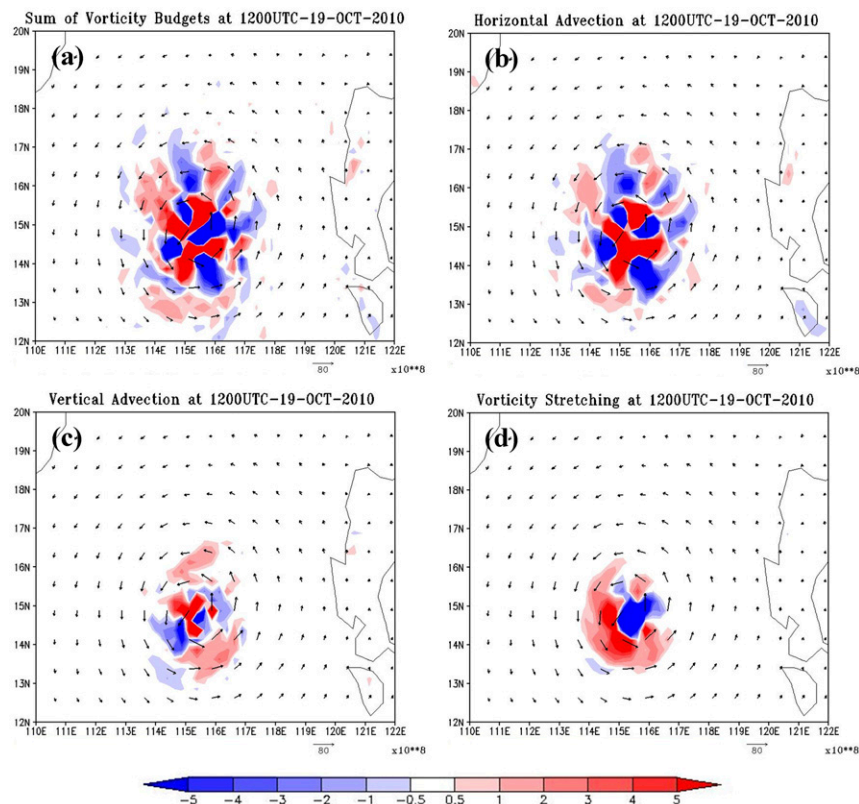


FIG. 15. (a) Sum of the budget terms in the vorticity equation averaged over 1–8-km height, and horizontal wind (m s^{-1}) at 3-km height, from the no_MJO simulation of Megi at 1200 UTC 19 Oct 2010. (b)–(d) As in (a), but for (b) horizontal vorticity advection, (c) vertical advection, and (d) vorticity stretching. All the panels are in units of $\text{s}^{-2} (\times 10^8)$.

the center. We have taken the vertical mean between 3 and 5 km for moderate Morakot and between 1 and 8 km for intense Megi and then computed their wavenumber-1 diagnostics. A radius of 400 km is chosen for both typhoons in computation of the translational speeds (C_x and C_y). Table 2 gives a list of the computed translational speeds derived from the vorticity tendency terms for both typhoons before and after their northward turning. The results from their no_MJO experiments are also included for comparisons with CTL.

Figure 16 shows the wavenumber-1 diagnostics of Morakot before turning at 1200 UTC 7 August 2009 for CTL. Intense northerly flow is mainly induced to the north and south of Morakot, in association with weaker northwestward flow in between that leads to a northward track at this time. Larger asymmetric positive vorticity is induced to the west of the vortex center (Fig. 16a), while intense upward motions are mainly produced to the south of the vortex center covering southern Taiwan and the southeastern offshore region (Fig. 16b). Wavenumber-1 motion exhibited by the vorticity tendency from different physical processes is

toward the positive maximum, with the corresponding translational speed of the vortex given in Table 2. Both horizontal advection (Fig. 16c) and vorticity tilting (Fig. 16f) lead to more northward movement, mostly counteracted by vertical advection (Fig. 16d) and vorticity stretching (Fig. 16e) with large southward components. The sum of vorticity budget terms (see Table 2) indicates a slightly north-northwestward movement ($C_x = -1.4 \text{ m s}^{-1}$ and $C_y = 2.1 \text{ m s}^{-1}$), which is consistent with the actual movement of Morakot at this time (see Fig. 7).

As Morakot takes a north-northwestward departure from northern Taiwan at 1800 UTC 7 August, the wavenumber-1 asymmetric flow in general is more southerly to the southeast and northwest of the inner vortex, while in between there is weaker southeasterly to southerly flow (Fig. 17a). Distributions with positive vorticity are aligned more north–south (cf. the earlier west–east orientation in Fig. 16a). Consequently, horizontal advection (Fig. 17c) becomes the most dominant contribution ($C_y = 4.7 \text{ m s}^{-1}$) to the northward movement. The upward motions remain dominant around

TABLE 2. Translational speeds of C_x and C_y (m s^{-1}) for Typhoons Morakot (2009) and Megi (2010) computed using the regression of wavenumber-1 vorticity changes due to different physical processes. Total budget also includes the solenoidal term and the term of Coriolis effect caused by vertical motions in the vorticity equation that are much smaller than the other four terms given in the table.

	Expt time	Horizontal advection	Vertical advection	Vorticity stretching	Vorticity tilting	Total budget
Morakot	CTL: 1200 UTC 7 Aug	2.7, 2.6	-2.9, -3.6	0.58, -1.5	-1.7, 4.6	-1.4, 2.1
	CTL: 1800 UTC 7 Aug	0.69, 4.7	0.63, -3.3	-2.0, -1.0	0.62, 1.0	-0.18, 1.4
	no_MJO: 0600 UTC 7 Aug	-0.2, -0.2	-6.1, -2.3	-3.1, -3.5	7.0, 6.9	-2.5, 0.76
Megi	CTL: 1200 UTC 19 Oct	-1.2, -0.69	0.21, -0.30	-1.2, 1.1	-1.8, 0.03	-4.0, 0.10
	CTL: 0000 UTC 20 Oct	2.6, 2.5	0.43, -0.33	-1.6, -1.0	-0.92, -0.03	0.52, 1.1
	no_MJO: 1200 UTC 19 Oct	-1.5, -2.1	-0.48, 0.03	-0.43, 0.79	-0.76, 0.19	-3.2, -1.2
	no_MJO: 0000 UTC 20 Oct	-3.6, 1.7	-0.29, 0.55	-0.01, 2.1	-0.90, 0.55	-4.8, 4.7

southern and southeastern Taiwan and farther southwest of Taiwan (Fig. 17b), thus leading to southward steering caused by vertical advection (not shown) and vorticity stretching (Fig. 17d). Vorticity tilting becomes less important with an induced small translational speed (see Table 2). At this time, Morakot departs mainly northward in agreement with the total budget tendency. As the MJO mode is removed, the primary northward flow around the vortex core of Morakot considerably weakens when closer to landfall (Fig. 17e). Horizontal advection becomes much weaker with two north-south bands so that it only introduces a very weak south-westward translational speed as seen in Table 2. Both vertical advection and vorticity stretching are intimately related to the intense upward motions west of Taiwan, and thus contribute mostly to the westward translation that is mainly counteracted by vorticity tilting. At this time, the total tendency budget supports a westward translational speed of 2.5 m s^{-1} , faster than that of CTL (1.4 m s^{-1}).

The wavenumber-1 diagnostics of vorticity budget shown in Fig. 18 also highlights the importance of the MJO mode in driving Megi northward. At 1200 UTC 19 October 2010 when Megi is about to take a north turn, the asymmetric flow is primarily eastward to the west of Megi and northward to the north and south (Fig. 18a). This is why the westward slowly moving Megi is going to take a north turn shortly. All the budget terms, except for vertical advection, mainly contribute to westward translation (see Table 2). Horizontal advection (Fig. 18a) indeed induces weak southward translation (-0.69 m s^{-1}), while vorticity stretching (Fig. 18b) contributes to larger northward translation (1.1 m s^{-1}). Vertical advection and vorticity stretching (figures not shown) appear to play a much less important role in the northward steering. At 0000 UTC 20 October, Megi is moving slowly northeastward as seen in Fig. 12, which appears to be supported by the wavenumber-1 asymmetric eastward to northeastward flow overwhelming outside of the vortex core (Fig. 18c). Horizontal advection becomes dominant at this time to steer

Megi northeastward, as exhibited by the associated wavenumber-1 structure. Vorticity stretching (Fig. 18d) shows more positive tendency to the southwest of the vortex center and thus induces a roughly southwestward translational speed. As the MJO mode is removed, there exists a pair of wavenumber-1 gyres to the north and south of the vortex at 1200 UTC 19 October (Fig. 18e). During the westward departure from the Philippines, the eastward asymmetric flow component west and east of the vortex core is largely reduced in the absence of the MJO. As seen in Fig. 12, Megi indeed is about to take a northwest turn at this time. The eastward flow of the wavenumber-1 gyres near the vortex center will not support a tendency of westward translation. However, Megi indeed is going to move west-northwestward at this time, consistent with the deeper (1–12 km) mean flow averaged in the vortex (Fig. 13c). On the other hand, all the budget terms favor a westward translation dominated by horizontal advection (Fig. 18e). Vorticity stretching also leads to primarily westward translation (Fig. 18f).

After the northwestward turn in the absence of the MJO, horizontal advection also leads to a west-northwestward translation at 0000 UTC 20 October, while vorticity stretching mainly contributes to a northward translation that is larger than those induced by the other terms (see Table 2). The wavenumber-1 flow in general is northward to northeastward outside of the vortex core and is northwestward near the southern flank of the vortex (not shown). The computed northwestward translation ($C_x = -4.8 \text{ m s}^{-1}$ and $C_y = 4.7 \text{ m s}^{-1}$) is in agreement with the actual movement of Megi (see Fig. 12). The westward movement of Megi at this time is considerably faster than that in the presence of the MJO.

The detailed structures and features of the vorticity tendency budget and vortex circulation associated with superintense Megi near its northward turning are quite different from those associated with moderate Morakot. In general, the vorticity tendency of Megi exhibits a more symmetric structure with quartic or quintic bands embedded in the inner vortex, while it is associated with

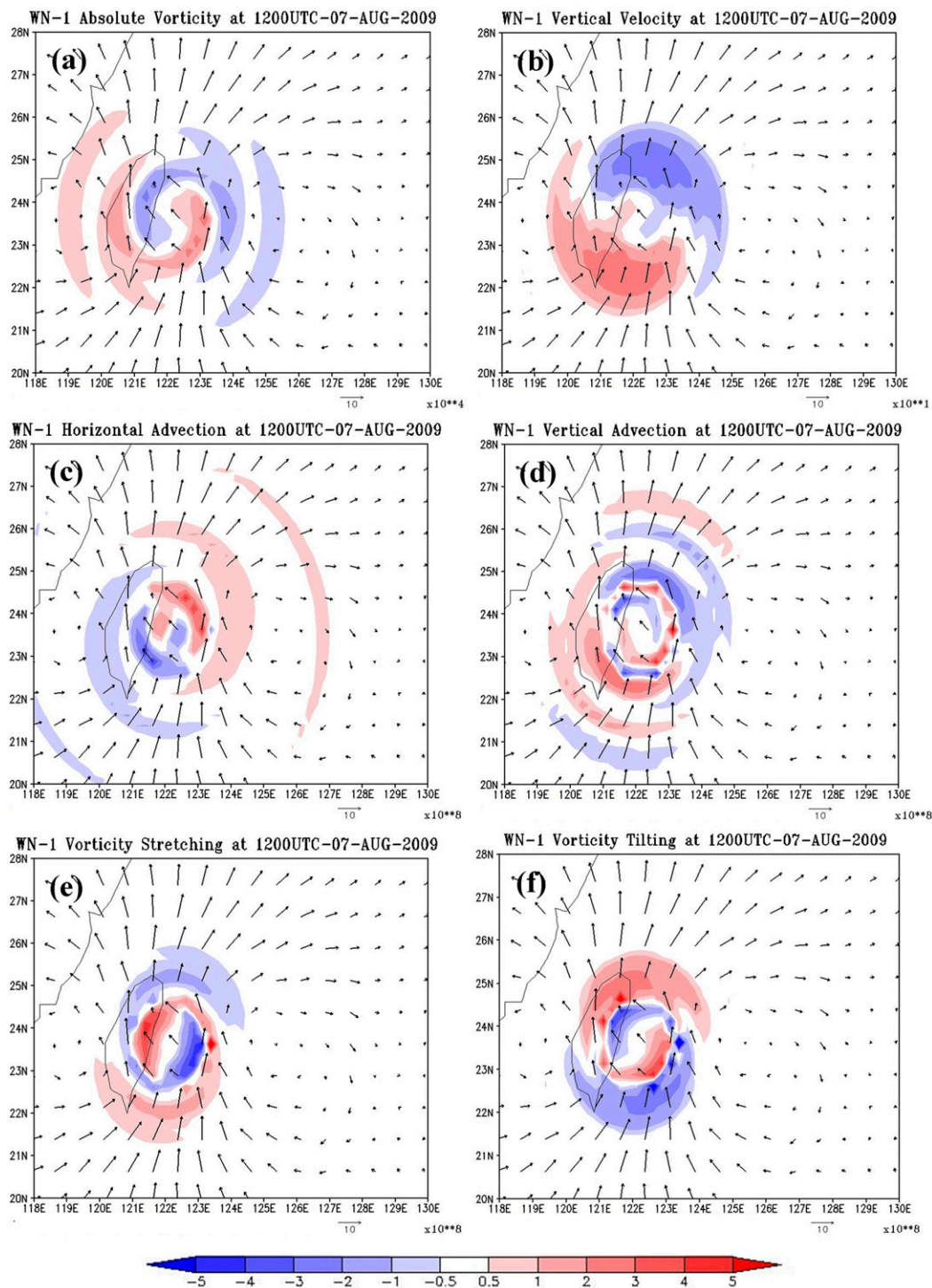


FIG. 16. (a) Wavenumber-1 vorticity and horizontal wind (m s^{-1}) averaged over 3–5-km height at 1200 UTC 7 Aug 2009 for CTL. (b) As in (a), but for the vertical velocity (m s^{-1} , $\times 10^1$), and the wavenumber-1 tendency budget (s^{-2} , $\times 10^8$) from (c) horizontal advection, (d) vertical advection, (e) vorticity stretching, and (f) vorticity tilting.

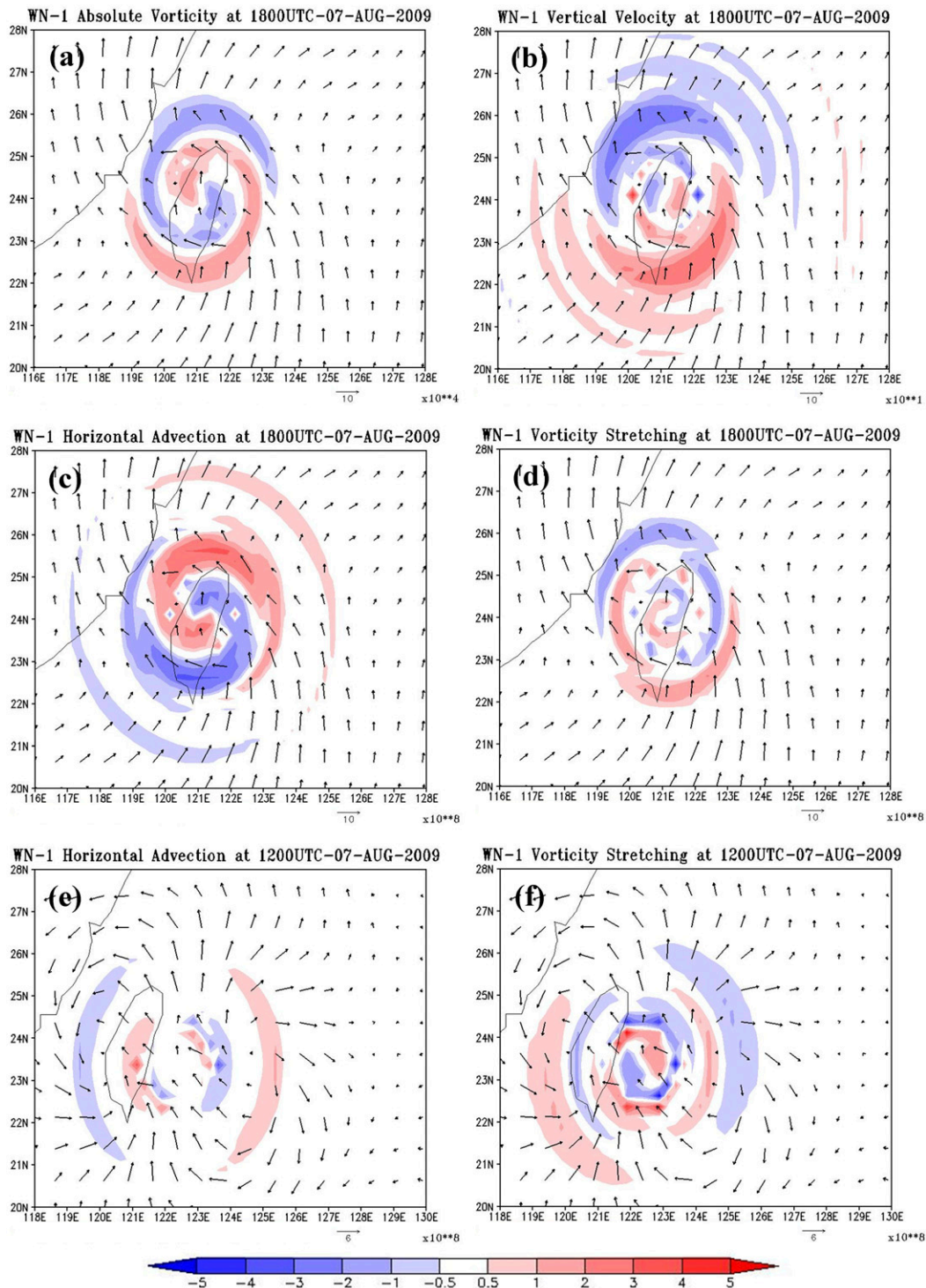


FIG. 17. (a) Wavenumber-1 vorticity and horizontal wind (m s^{-1}) averaged over 3–5-km height at 1800 UTC 7 Aug 2009 for CTL. (b) As in (a), but for the vertical velocity ($\text{m s}^{-1} \times 10^1$), and the wavenumber-1 tendency budget ($\text{s}^{-2} \times 10^8$) from (c) horizontal advection, and (d) vorticity stretching. (e),(f) As in (c),(d), but at 1200 UTC 7 Aug 2009 for no_MJO.

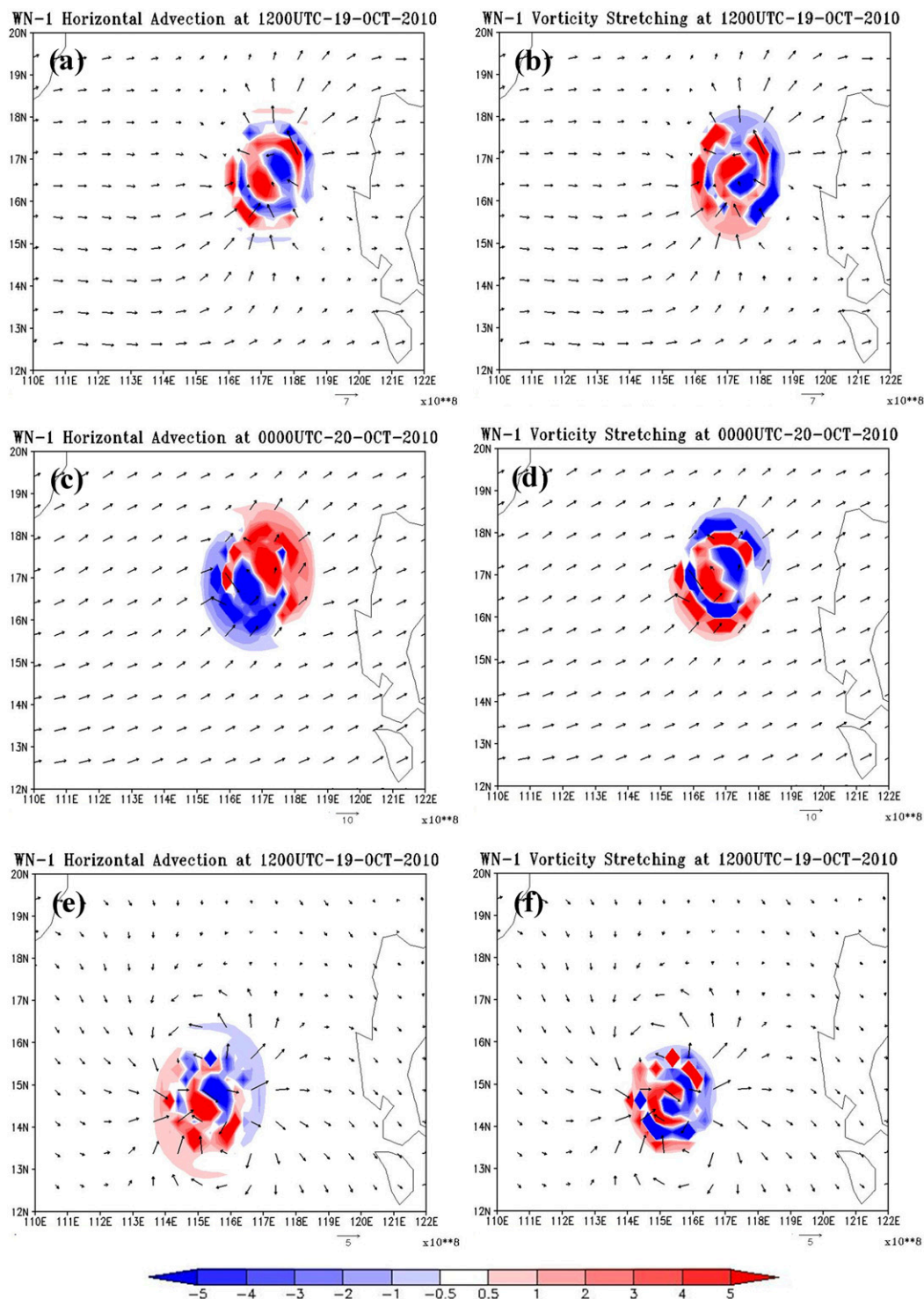


FIG. 18. The wavenumber-1 tendency budget ($s^{-2}, \times 10^8$) from (a) horizontal advection and (b) vorticity stretching at 1200 UTC 19 Oct 2010 for CTL. (c),(d) As in (a),(b), but at 0000 UTC 20 Oct 2010 for CTL. (e),(f) As in (a),(b), but at 1200 UTC 19 Oct 2010 for no_MJO.

propagating banded disturbances away from the vortex core of Morakot. In spite of some differences in the vorticity tendency budget, their northward movement is commonly dictated by the leading positive horizontal vorticity advection. For superintense Megi, vertical vorticity advection and vorticity tilting have important contributions but only around the inner vortex core, and thus do not impose a strong steering compared to those for moderate Morakot (see Table 2). For Morakot, positive vorticity tilting becomes relatively more important before turning. This can be attributed to the slantwise structure of Morakot that tends to produce a northward translation mostly counteracted by southward translation from vertical advection. Vorticity stretching tends to support the westward acceleration of Megi but becomes more complicated for Morakot due to the effect of the CMR. This topographical effect turns out to retard the northward translation of Morakot near and after landfall. The vorticity budget diagnostics in this study help explain the track evolution of Morakot, and may complement other studies that demonstrated the existence of reverse localized forcing due to the induced strong latent heating in the vicinity of southern Taiwan (e.g., Chien and Kuo 2011; Wang et al. 2012).

7. Conclusions

Numerical experiments are conducted to investigate the influences of the various large-scale flows on the track evolution of typhoons, in particular the impacts of MJO variations. Two typhoons are examined in this study, moderate Morakot (2009) and superintense Megi (2010). The numerical simulations employ a recently developed global model MPAS, which has a variable resolution of 60–15 km with the highest resolution of 15 km centered over the Taiwan area in this study. Use of the global model helps eliminate the impacts of lateral boundary conditions on regional models, and its performances are justified by comparisons with the regional model WRF using the same physical schemes and initial conditions as in the simulations of Morakot.

Based on the wavelet power spectrum that shows three dominant modes associated with the convection in the vicinity of Taiwan around the middle 2009, the modes of 10, 10–20, and 20–60 days in the flow are filtered from the global reanalysis to provide the flow components without the synoptic-scale flow (no_SYN), without the quasi-biweekly flow (no_QBW), and without the MJO monsoonal flow (no_MJO), respectively. In the control experiment (with the unfiltered flow), the MPAS model well captures the northward track of Morakot and the patterns of severe rainfall over southern Taiwan. Sensitivity experiments show the different

roles of the synoptic-scale (SYN), the QBW-scale, and the MJO-scale flows in affecting the track evolution of Morakot. In the absence of larger-scale monsoonal flow (no_MJO), the simulated Morakot in general moves westward without the observed north turn after landfall. On the other hand, there exist increased southwesterly wind increments from the South China Sea to the east of Taiwan in the western North Pacific when the MJO mode is enhanced by 50%, thus resulting in an abrupt north turn of Morakot at a much earlier time than observed. The simulated Morakot track under the intact MJO lies in between MJO+50% and MJO–50%, which suggests that the monsoonal flow is intimately related to the northward turning after landfall, in agreement with Liang et al. (2011) based on WRF simulations.

To highlight the role of the MJO in the typhoon evolution, we conducted the other experiment for superintense Typhoon Megi (2010) that also took an abrupt north turn after a westward passage over the northern Philippines. The sensitivity experiments using MPAS indicates that Megi cannot take such a north turn when the MJO mode is filtered out from the model initial condition, which is somewhat similar to the impact of the ISO component (10–60 days) based on WRF simulations (Bi et al. 2015). The extra QBW mode contained in their ISO leads to a less northward movement at later stages compared to that from the MJO mode in this study. In general, the impacts of MJO variations on the track evolution of Megi are similar to Morakot. For example, Megi also takes an earlier north turn when the MJO intensity is further increased by 50%. According to our analysis of the MJO mode from the sensitivity experiments, we note that the northward turning of both typhoons is intimately linked with the coalescence of the monsoon gyre with the typhoon center.

To further understand how the movement of both Morakot and Megi is sensitive to the MJO, the typhoon circulation and associated vorticity tendency budget are diagnosed from the MPAS 15-km simulations. The importance of each budget term is assessed in terms of its contribution to the vortex translation, which is determined by the regression of a decomposed wavenumber-1 vorticity tendency. In the presence of the MJO mode, strong wavenumber-1 southerly flow is induced around the vortex, leading to the northward turning of both typhoons mainly in response to the more dominant positive horizontal vorticity advection to the north of the vortex center. The dominance of horizontal vorticity advection in steering Megi in our study for the impact of MJO is in agreement with that for the impact of ISO (Bi et al. 2015). Without the MJO, horizontal vorticity advection tends to produce westward tendency and/or reduce northward

tendency for both typhoons. However, vorticity tilting appears to be relatively more important for Morakot (due to a slantwise structure), and primarily contributes to a northward motion before turning. In addition, positive vorticity stretching and vertical advection are significant in the vicinity of southern Taiwan (due to the effects of the Central Mountain Range) and thus tend to retard the departing Morakot. The vortex dynamics and evolution of two distinct typhoons in association with the common influence of MJO are first compared and illuminated by this study.

Acknowledgments. This study was supported by the Ministry of Science and Technology (MOST) Grant MOST-2111-M-008-019 (Taiwan).

APPENDIX A

The Equation of Vertical Vorticity

The equation for absolute vorticity ($\zeta + f$) in the height coordinate is given by

$$\begin{aligned} \frac{\partial}{\partial t}(\zeta + f) = & -\mathbf{U} \cdot \nabla(\zeta + f) - (\zeta + f)(u_x + v_y) \\ & - (w_x v_z - w_y u_z) + \frac{1}{\rho^2}(\rho_x p_y - \rho_y p_x) \\ & + (F_{ux} - F_{uy}) + \frac{\partial(2\Omega \cos\phi w)}{\partial y}, \end{aligned} \quad (\text{A1})$$

where $\zeta = v_x - u_y$ represents relative vorticity, $f = 2\Omega \sin\phi$ is the planetary vorticity at the latitude ϕ , \mathbf{U} is the wind vector with the three directional components (u, v, w), ρ is density, p is pressure, and F_u and F_v are turbulent mixing in the u - and v -momentum equations, respectively. The term on the left-hand side of (A1) represents the local time change rate of the absolute vorticity ($\zeta + f$), and the terms on the right-hand side represent contributions from vorticity advection, vorticity stretching, vorticity tilting, solenoidal effects, turbulent diffusion (mostly in the PBL), and Coriolis effects due to vertical motions, respectively. The last term in (A1) is usually much smaller than other terms but is retained since it is included in the MPAS horizontal momentum equation (Skamarock et al. 2012). All the terms in (A1) can be transformed to the hybrid coordinate in (1) or calculated in the height coordinate. For convenience, we interpolate the model variables to spherical coordinates spacing by 0.25° in latitude by 0.25° in longitude and 200 m in height. The relative vorticity then is computed as $\zeta = 1/r \cos\phi[(\partial v/\partial \lambda) - (\partial u \cos\phi/\partial \phi)]$, where r is the radius of the spherical planet and λ is the longitude. Both F_u and F_v are output on the native hybrid coordinate and are interpolated to the height coordinate.

APPENDIX B

Wavenumber-1 Diagnostics of Vorticity Tendency

Diagnostics of wavenumber-1 vorticity changes can provide useful information for understanding the typhoon movement. We also apply the regression method to quantify the translational speed of the typhoon as caused by different physical processes in the vorticity equation, following Wu and Wang (2000) and Hsu et al. (2013). Given the decomposed wavenumber-1 vorticity changes, the east–west and north–south components are given, respectively, by

$$C_x = -\frac{\sum_{i=1}^N \left(\frac{\partial \bar{\zeta}_0}{\partial x} \right)_i \left(\frac{\partial \bar{\zeta}_1}{\partial t} \right)_i}{\sum_{i=1}^N \left(\frac{\partial \bar{\zeta}_0}{\partial x} \right)_i^2}, \quad (\text{B1})$$

and

$$C_y = -\frac{\sum_{i=1}^N \left(\frac{\partial \bar{\zeta}_0}{\partial y} \right)_i \left(\frac{\partial \bar{\zeta}_1}{\partial t} \right)_i}{\sum_{i=1}^N \left(\frac{\partial \bar{\zeta}_0}{\partial y} \right)_i^2}, \quad (\text{B2})$$

where the bar represents vertical mean; indices 0 and 1 indicates the symmetric and wavenumber-1 components, respectively, for any grid point i within a specified radius of the typhoon center; and the wavenumber-1 vorticity tendency is contributed from each term on right-hand side of (A1).

REFERENCES

- Bi, M., T. Li, M. Peng, and X. Shen, 2015: Interactions between Typhoon Megi (2010) and a low-frequency monsoon gyre. *J. Atmos. Sci.*, **72**, 2682–2702, doi:[10.1175/JAS-D-14-0269.1](https://doi.org/10.1175/JAS-D-14-0269.1).
- Carr, L. E., and R. L. Elsberry, 1990: Observational evidence for predictions of tropical cyclone propagation relative to environmental steering. *J. Atmos. Sci.*, **47**, 542–546, doi:[10.1175/1520-0469\(1990\)047<0542:OEFPT>2.0.CO;2](https://doi.org/10.1175/1520-0469(1990)047<0542:OEFPT>2.0.CO;2).
- , and —, 1995: Monsoonal interactions leading to sudden tropical cyclone track changes. *Mon. Wea. Rev.*, **123**, 265–290, doi:[10.1175/1520-0493\(1995\)123<0265:MILTST>2.0.CO;2](https://doi.org/10.1175/1520-0493(1995)123<0265:MILTST>2.0.CO;2).
- Chen, T.-C., and C.-C. Wu, 2016: The remote effect of Typhoon Megi (2010) on the heavy rainfall over northeastern Taiwan. *Mon. Wea. Rev.*, **144**, 3109–3131, doi:[10.1175/MWR-D-15-0269.1](https://doi.org/10.1175/MWR-D-15-0269.1).
- Chien, F.-C., and H.-C. Kuo, 2011: On the extreme rainfall of Typhoon Morakot (2009). *J. Geophys. Res.*, **116**, D05104, doi:[10.1029/2010JD015092](https://doi.org/10.1029/2010JD015092).
- Duchon, C. E., 1979: Lanczos filtering in one and two dimensions. *J. Appl. Meteor.*, **18**, 1016–1022, doi:[10.1175/1520-0450\(1979\)018<1016:LFIOAT>2.0.CO;2](https://doi.org/10.1175/1520-0450(1979)018<1016:LFIOAT>2.0.CO;2).

- Fang, X., Y.-H. Kuo, and A. Wang, 2011: The impacts of Taiwan topography on the predictability of Typhoon Morakot's record-breaking rainfall: A high-resolution ensemble simulation. *Wea. Forecasting*, **26**, 613–633, doi:[10.1175/WAF-D-10-05020.1](https://doi.org/10.1175/WAF-D-10-05020.1).
- Ge, X., T. Li, S. Zhang, and M. Peng, 2010: What causes the extremely heavy rainfall in Taiwan during Typhoon Morakot (2009)? *Atmos. Sci. Lett.*, **11**, 46–50.
- Hack, J. J., and W. H. Schubert, 1981: Lateral boundary conditions for tropical cyclone models. *Mon. Wea. Rev.*, **109**, 1404–1420, doi:[10.1175/1520-0493\(1981\)109<1404:LBCFTC>2.0.CO;2](https://doi.org/10.1175/1520-0493(1981)109<1404:LBCFTC>2.0.CO;2).
- Hagos, S., R. Leung, S. A. Rauscher, and T. Ringler, 2013: Error characteristics of two grid refinement approaches in aquaplanet simulations: MPAS-A and WRF. *Mon. Wea. Rev.*, **141**, 3022–3036, doi:[10.1175/MWR-D-12-00338.1](https://doi.org/10.1175/MWR-D-12-00338.1).
- Holland, G. J., 1983: Tropical cyclone motion: Environmental interaction plus a beta effect. *J. Atmos. Sci.*, **40**, 328–342, doi:[10.1175/1520-0469\(1983\)040<0328:TCMEIP>2.0.CO;2](https://doi.org/10.1175/1520-0469(1983)040<0328:TCMEIP>2.0.CO;2).
- Hong, C.-C., M.-Y. Lee, H.-H. Hsu, and J.-L. Kuo, 2010: Role of submonthly disturbance and 40–50 day ISO on the extreme rainfall event associated with Typhoon Morakot (2009) in southern Taiwan. *Geophys. Res. Lett.*, **37**, L08805, doi:[10.1029/2010GL042761](https://doi.org/10.1029/2010GL042761).
- Hsu, L.-H., H.-C. Kuo, and R. G. Fovell, 2013: On the geographic asymmetry of typhoon translation speed across the mountainous island of Taiwan. *J. Atmos. Sci.*, **70**, 1006–1022, doi:[10.1175/JAS-D-12-0173.1](https://doi.org/10.1175/JAS-D-12-0173.1).
- Huang, C.-Y., C.-S. Wong, and T.-C. Yeh, 2011: Extreme rainfall mechanisms exhibited by Typhoon Morakot (2009). *Terr. Atmos. Oceanic Sci.*, **22**, 613–632, doi:[10.3319/TAO.2011.07.01.01\(TM\)](https://doi.org/10.3319/TAO.2011.07.01.01(TM)).
- Klemp, J. B., 2011: A terrain-following coordinate with smoothed coordinate surfaces. *Mon. Wea. Rev.*, **139**, 2163–2169, doi:[10.1175/MWR-D-10-05046.1](https://doi.org/10.1175/MWR-D-10-05046.1).
- Ko, K. C., and H. H. Hsu, 2009: ISO modulation on the submonthly wave pattern and recurving tropical cyclones in the tropical western North Pacific. *J. Climate*, **22**, 582–599, doi:[10.1175/2008JCLI2282.1](https://doi.org/10.1175/2008JCLI2282.1).
- Lander, M., 1994: Description of a monsoon gyre and its effects on the tropical cyclones in the western North Pacific during August 1991. *Wea. Forecasting*, **9**, 640–654, doi:[10.1175/1520-0434\(1994\)009<0640:DOAMGA>2.0.CO;2](https://doi.org/10.1175/1520-0434(1994)009<0640:DOAMGA>2.0.CO;2).
- Li, R.-C., and W. Zhou, 2013: Modulation of western North Pacific tropical cyclone activity by the ISO. Part II: Tracks and landfalls. *J. Climate*, **26**, 2919–2930, doi:[10.1175/JCLI-D-12-00211.1](https://doi.org/10.1175/JCLI-D-12-00211.1).
- Liang, J., L. Wu, X. Ge, and C.-C. Wu, 2011: Monsoonal influence on Typhoon Morakot (2009). Part II: Numerical study. *J. Atmos. Sci.*, **68**, 2222–2235, doi:[10.1175/2011JAS3731.1](https://doi.org/10.1175/2011JAS3731.1).
- Liebmann, B., H. H. Hendon, and J. D. Glick, 1994: The relationship between tropical cyclones of the western Pacific and Indian Oceans and the Madden-Julian oscillation. *J. Meteor. Soc. Japan*, **72** (3), 401–412.
- Ling, Z., Y. Wang, and G. Wang, 2016: Impact of intraseasonal oscillations on the activity of tropical cyclones in summer over the South China Sea. Part I: Local tropical cyclones. *J. Climate*, **29**, 855–868, doi:[10.1175/JCLI-D-15-0617.1](https://doi.org/10.1175/JCLI-D-15-0617.1).
- Park, S.-H., J. B. Klemp, and W. C. Skamarock, 2014: A comparison of mesh refinement in the global MPAS-A and WRF models. *Mon. Wea. Rev.*, **142**, 3614–3634, doi:[10.1175/MWR-D-14-00004.1](https://doi.org/10.1175/MWR-D-14-00004.1).
- Skamarock, W. C., and Coauthors, 2008: A description of the Advanced Research WRF version 3. NCAR Tech. Note NCAR/TN-475+STR, 113 pp., doi:[10.5065/D68S4MVH](https://doi.org/10.5065/D68S4MVH).
- , J. B. Klemp, M. G. Duda, L. D. Fowler, S.-H. Park, and T. D. Ringler, 2012: A multiscale nonhydrostatic atmospheric model using centroidal Voronoi tessellations and C-grid staggering. *Mon. Wea. Rev.*, **140**, 3090–3105, doi:[10.1175/MWR-D-11-00215.1](https://doi.org/10.1175/MWR-D-11-00215.1).
- Torrence, C., and G. P. Compo, 1998: A practical guide to wavelet analysis. *Bull. Amer. Meteor. Soc.*, **79**, 61–78, doi:[10.1175/1520-0477\(1998\)079<0061:APGTWA>2.0.CO;2](https://doi.org/10.1175/1520-0477(1998)079<0061:APGTWA>2.0.CO;2).
- Wang, C.-C., H.-C. Kuo, Y.-H. Chen, H.-L. Huang, C.-H. Chung, and K. Tsuboki, 2012: Effects of asymmetric latent heating on typhoon movement crossing Taiwan: The case of Morakot (2009) with extreme rainfall. *J. Atmos. Sci.*, **69**, 3172–3196, doi:[10.1175/JAS-D-11-0346.1](https://doi.org/10.1175/JAS-D-11-0346.1).
- Wheeler, M. C., and H. H. Hendon, 2004: An all-season real-time multivariate MJO index: Development of an index for monitoring and prediction. *Mon. Wea. Rev.*, **132**, 1917–1932, doi:[10.1175/1520-0493\(2004\)132<1917:AARMMI>2.0.CO;2](https://doi.org/10.1175/1520-0493(2004)132<1917:AARMMI>2.0.CO;2).
- Wu, L., and B. Wang, 2000: A potential vorticity tendency diagnostic approach for tropical cyclone motion. *Mon. Wea. Rev.*, **128**, 1899–1911, doi:[10.1175/1520-0493\(2000\)128<1899:APVTDA>2.0.CO;2](https://doi.org/10.1175/1520-0493(2000)128<1899:APVTDA>2.0.CO;2).
- , J. Liang, and C.-C. Wu, 2011: Monsoonal influence on Typhoon Morakot (2009). Part I: Observational analysis. *J. Atmos. Sci.*, **68**, 2208–2221, doi:[10.1175/2011JAS3730.1](https://doi.org/10.1175/2011JAS3730.1).